1-1-2013

Thermal Dose Based Monitoring Of Laser Interstitial Thermal Therapy For Prostate Cancer

David Dalla Rosa
Ryerson University

THERMAL DOSE BASED MONITORING OF LASER INTERSTITIAL

THERMAL THERAPY FOR PROSTATE CANCER

By

David Dalla Rosa

B. Sc. Medical Physics, Ryerson University, 2010

A thesis

presented in partial fulfillment

of the requirements for the degree

of Master of Science

in the program of

Biomedical Physics

Toronto, Ontario, Canada, 2013

I hereby declare that I am the sole author of this thesis. This is a true copy of the thesis, including any required final revisions, as accepted by my examiners.

I authorize Ryerson University to lend this thesis to other institutions or individuals for the purpose of scholarly research.

I further authorize Ryerson University to reproduce this thesis by photocopying or by other means, in total or in part, at the request of other institutions or individuals for the purpose of scholarly research.

I understand that my thesis may be made electronically available to the public

Thermal Dose Based Monitoring of Laser Interstitial Thermal Therapy for Prostate

Cancer

Master of Science, 2013

David Dalla Rosa

Biomedical Physics

Ryerson University

Abstract

The two most commonly used methods of treatment monitoring and prediction in thermal therapy are the temperature threshold method and the cumulative equivalent minutes at 43°C (CEM_{43}) thermal dose model. A newly introduced thermal dose model, the improved cumulative equivalent minutes at 43°C ($iCEM_{43}$), has been preliminary shown to be more consistent than the CEM_{43} thermal dose model.

Data from an ongoing clinical trial for laser treatment of low-grade prostate cancer was used to test the consistency of all three methods. Firstly, threshold values required to match the post-treatment damage were predicted and the $iCEM_{43}$ dose model was more consistent than the CEM_{43} dose model, while the temperature threshold method was the most consistent. Secondly, a threshold value was chosen for each method and the damage was predicted and compared to the known damage where the $iCEM_{43}$ dose model outperformed both the CEM_{43} dose model and the temperature threshold method.

Acknowledgements

First and for most I would like to acknowledge my thesis supervisor Dr. J. Carl Kumaradas for all the support and guidance which he provided for me. No matter what the situation, I had full confidence going to him for help and support knowing that he had probably encountered a similar situation as both a researcher and supervisor. Secondly, I would like to acknowledge the efforts put forth by the members of my supervisory committee Dr. Emily Heath and Dr. Michael Kolios. The input, thoughts, and questions provided by them were an integral part of the completion of this research.

Furthermore, I would like to thank Dr. John Trachtenberg for gratefully sharing the data from his ongoing clinical trials which made this research possible. A special thanks to Sean Davidson for his efforts in the screening and exporting of the data from the treatments, and providing them to me in a timely manner. I would also like to thank Dr. Marshall Sussman for his expertise and assistance with regards to the Magnetic Resonance Imaging, especially with regards to his work on artifact determination.

Lastly, I would like to thank my friends and family for all their support through this entire endeavour. Their patience with me during times of stress did not go unnoticed and was very much appreciated.

Table of Contents

List of Tables

List of Figures

1. Introduction

1.1. Prostate Cancer

According to Prostate Cancer Canada, prostate cancer is the most common cancer amongst Canadian men. Each day an average of 73 Canadian men will be diagnosed with prostate cancer and 11 will succumb to the disease [1]. Depending on the severity, there are a number of different treatment options available to patients. These include radical prostatectomy, radiation therapy (external beam and brachytherapy), hormone therapy, and chemotherapy.

Radical prostatectomy is a surgery that removes the entire prostate gland as well as some of the seminal vesicles and a part of the urethra. This is viable option for cases where the cancer has not spread outside of the prostate. There are a number of possible undesirable side effects of this surgery, including but not limited to, erectile dysfunction. Another important side effect of this procedure is that it will result in infertility [2].

Radiation therapy is also a common treatment option, and is sometimes accompanied by a prostatectomy following completion of therapy. There are two main types of radiation therapy, external beam therapy and brachytherapy. External beam therapy utilises radiation (gamma rays, x-rays, beta particles, or ions) produced outside the body to localize exposure of a prostate region which interferes with cell division, thus killing cancer cells. Long-term side effects may include infertility and erectile dysfunction (which occurs in 50% of cases). Brachytherapy is more invasive, as it involves surgery to implant radiation sources inside the prostate. For lower grade cancer localized in the prostate, radioactive seeds are implanted which slowly irradiate the prostate over the course of months. For high-grade cancer patients, catheters are inserted in the

tumour site and these catheters are wired to a radioactive source (source is kept in a sealed and shielded), delivering a higher dose to the region over a shorter length of time. This treatment lasts about 20 minutes and is sometimes given over a few days to eliminate the need for external beam radiation. The side-effects of brachytherapy are very similar to those of external beam radiation therapy [2].

Hormone therapy is generally used when the cancer has already spread outside of the prostate as well as when there is recurrence of prostate cancer following another form of therapy. Hormone therapy works by depriving the body of the androgens that cancer cells require for growth. Hormone therapy is also used prior to a local treatment to reduce the tumour size in the hopes of increasing the efficacy of the local treatment. Furthermore, following a surgery or radiation to remove a tumour, hormone therapy can be used to treat any cancerous cells that may remain. There are a number of side effects that are possible from this treatment including, erectile dysfunction, loss of energy, loss of muscle mass, irritability, and osteoporosis [2].

Chemotherapy is the use of drugs to treat cancer, and is usually used to treat recurring or metastatic prostate cancer if hormone therapy is no longer effective. Chemotherapy drugs affect both healthy and cancer cells, after administration of the drugs, cancer cells struggle to recover from the exposure to the drugs, whereas the healthy cells tend to regenerate better. It is typically used to delay the spread of cancer and prolong life in the late stages of cancer. Some common side effects include nausea, vomiting, hair loss, and infertility [2].

There is ongoing research of newer treatment options. Most of the research is on trying to limit unwanted side effects and improving the quality of life following treatment as compared to the traditional treatment options. One example is transurethral ultrasound therapy being researched by a research group at Sunnybrook Hospital in Toronto headed by Dr. K. Siddiqui

and Dr. R. Chopra [3]. Another example is transrectal high intensity focused ultrasound (HIFU), which is in wide clinical use in Europe and has recently begun to be seen elsewhere in the world, including North America [4]. This procedure involves an ultrasound probe inserted into the patient's rectum that radiates high frequency ultrasound waves to heat and destroy the prostate tissue while minimizing heat exposure to the rectum [4]. This procedure is typically used in place of radical prostatectomy, as it decreases the risks of many of the unwanted side effects akin to prostate gland removal. Another treatment, that will be looked at in greater detail in this thesis, is the work being done at Princess Margaret Hospital by Dr. U. Lindner and Dr. J. Trachtenberg, who are running a clinical trial using laser interstitial thermal therapy to treat low grade localized prostate cancer [5]. The advantages of this treatment over traditional methods are the decrease in the occurrence of specific undesirable side effects such as infertility and erectile dysfunction. This particular clinical trial is explained in greater detail in **Section 3.1** of this thesis.

1.2. Thermal Therapy

The advancement of technology leads to newer ways of solving issues and problems faced in every aspect of the world. The field of medicine is at the forefront of this as when new technology arises it gives opportunity for improving and even creating new novel procedures. An ever growing field is the treatment or removal of unwanted or infected tissues, in particular as it pertains to cancerous tumours. One particular area of interest is the utilization of heat to destroy tumours and other unwanted tissues and is referred to as thermal therapy. In cancer treatment, thermal therapy is divided into two distinct categories, hyperthermia and coagulative thermal therapy. Hyperthermia came first, which is the use of heat in conjunction with other treatment modalities (i.e. radiation and chemotherapy). The targeted tissue is heated to roughly

42°C to 46°C to increase the amount of tissue death by increasing its sensitivity to the traditional modality being utilized (increase radiosensitivity, increased drug uptake, etc.) [6]. As technology improved, the ability to controllably heat targeted tissues to higher temperatures became possible which gave rise to the field of coagulative thermal therapy. Coagulative thermal therapy is the utilization of heat alone to destroy the targeted tissue. When tissue is heated to temperatures in excess of 60°C protein denaturation occurs, referred to as thermal coagulative necrosis and is the main mechanism of tissue death [7]. A number of different heating techniques have already been investigated, including microwaves [8], ultrasound [4],[3], and lasers [9].

1.3. Preliminary Comparison of Thermal Dose Models

Later in this thesis in **Section 2.1.4** a new thermal dose model will be presented as first introduced by Hisham Assi in his Master's thesis [10]. The aim of his work was to compare the consistency of his improved equivalent minutes at 43°C (iCEM$_{43}$) and the current cumulative equivalent minutes at 43°C (CEM$_{43}$) thermal dose models. Assi's work included *ex-vivo* bovine liver heating experiments using laser energy. Each experiment involved the creation of six thermal lesions on the surface of *ex-vivo* bovine liver tissue. A thermal camera was used to acquire and record the surface temperature map for the duration of each of lesions. Different exposure times were used to create lesions of different sizes, and following the procedure an optical image of the six lesions was acquired. Using the acquired temperature histories for each lesion, t_{43} (CEM$_{43}$) and t'_{43} (iCEM$_{43}$) dose values in equivalent minutes were calculated.

To test the damage prediction of each of the dose models, tissue whitening was looked at, as thermal damage in bovine liver tissue is accompanied by the change of optical properties. An

intensity threshold for the optical image was selected, where anything greater than this intensity was made white and everything else black. In other words, a binary representation of the lesions was created, where the white pixels represented the irreparably damaged regions. For each lesion, using the dose maps created by both dose models, the dose contour enclosing the same area as the white region in the binary representation of damage was determined. In an ideal world the dose thresholds for each lesion would be the same. The results of this portion of Assi's work are shown in **Figure 1.1**, where it can easily be seen that the iCEM$_{43}$ thermal dose model is more consistent in its dose prediction as opposed to the CEM$_{43}$ model. This was a good first step into the testing of the iCEM$_{43}$ thermal dose model, however, more in-depth work, especially in more clinically relevant situations is needed.
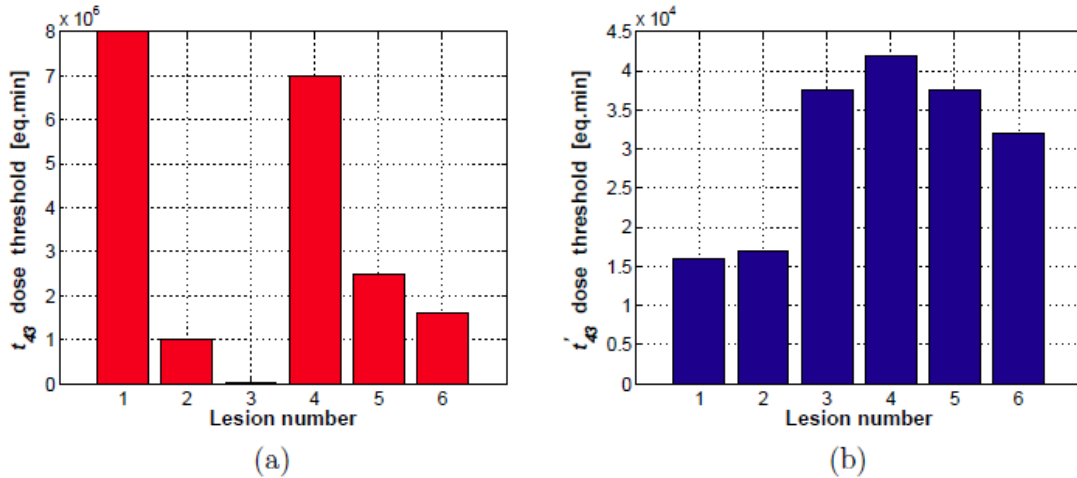
Figure 1.1: Calculated dose thresholds estimating the regions of damage for each of the six lesions using the (a) t_{43} and (b) t'_{43} thermal dose models. Reproduced from [10].

1.4. Hypothesis and Specific Aims

As indicated by the preliminary work by Assi, the newly introduced iCEM$_{43}$ thermal dose model could improve the predicted outcomes of thermal therapies. The logical next step was to look into more clinically suitable experiments to further test the dose models. Looking at the

three models described in later sections, temperature threshold, CEM_{43}, and $iCEM_{43}$ their consistency in predicting thermal dose was investigated in a more clinically suitable manner. Furthermore, Assi's work did not include the temperature threshold method in its comparison of models, whereas the work presented in this thesis will. It is hypothesized that the newly introduced $iCEM_{43}$ thermal dose model will be more clinically suitable in predicting the damage outcomes in coagulative thermal therapy than both the CEM_{43} dose model and the temperature threshold technique.

This thesis will aim to determine the relative consistencies of all three treatment monitoring techniques, and determine which one is most suitable for laser thermal therapy of prostate cancer. Secondly, the universality of the three methods will be determined, in that using a single threshold value for each method across a number of patients to predict the region of damage as compared to the damage seen post-treatment.

2. Theory

2.1. Treatment Monitoring

In thermal therapy, as with other cancer treatment techniques, the goal is to destroy the unhealthy (tumour) tissue, while limiting the damage to the surrounding healthy tissues and organs. Determining the extent of damage within the target is not a straightforward task, and thus treatment monitoring techniques are needed. Diagnostic ultrasound has been investigated and it is both non-invasive and has real-time feedback [11]. However, after treatment the echogenic region becomes heterogeneous, thus limiting its usefulness [12]. Computed Tomography (CT) is a very useful tool in both the pre and post treatment aspects, however due to the required computing time, real-time contrast enhanced CT maps are not a viable option [13]. Another monitoring technique that has been investigated is that of optical point-based monitoring. When tissue coagulation occurs, there is a change in the optical properties thus healthy and coagulated tissue can be detected as differences in the light intensity profile at given points [14]. The most widely used techniques for monitoring the damage throughout the procedure are based on the temperatures reached within the target. One simple strategy is the use of thermocouples placed in strategic locations that monitor the temperature in real-time at these particular locations. Typically these thermocouples are placed in areas such as the tumour boundary or nearby healthy organs, and the temperature information can then be used to dictate the progress of the treatment [15]. The work described in this thesis uses magnetic resonance imaging (MRI) to monitor the temperature during treatment and uses this temperature information to formulate predictions for the region of damage.

2.1.1. MRI Thermometry

The basis of magnetic resonance imaging (MRI) is the presence of a large number of water molecules in human tissues. The nuclei of hydrogen atoms in the water molecules act as small magnets. Contrast in MRI images is the result of differences in tissue relaxation properties. T1-weighted images are based on the fact that the nuclear spins from hydrogen atoms in water molecules lose energy to the lattice, resulting in realignment with the magnetic field. T2-weighted images are based on the interaction between the spinning molecules, often referred to as spin-spin relaxation [16].

The most common used method for MRI thermometry is known as Proton Resonance Frequency (PRF) temperature mapping. Changes in temperature lead to changes to the local magnetic field as the result of changes in electronic shielding, which then affects the nucleus and its resonance frequency. PRF temperature mapping is done by finding the difference in a particular phase-map from a baseline one, acquired prior to heat energy deposition. The protons from the hydrogen atoms in water oscillate with a particular resonant frequency. Upon heating the resonant of the protons (hydrogen nucleus) changes and this change in frequency can be expressed as a change in phase. It is this phase change, stemming from the change in proton resonant frequency that is the basis for thermometry. The temperature of a voxel can be expressed as:

$$T = T_0 + \frac{\Delta\emptyset}{\gamma B_0 \tau_E \alpha} \qquad \textbf{2.1}$$

where B_0 is the magnetic field strength, τ_E is the echo time, γ is the gyro magnetic constant, α is the proportionality constant, $\Delta\emptyset$ is the phase difference between the current map and the baseline

(prior to heating), and T_0 is the initial temperature [16]. The value for α has been shown to be independent of tissue type and has been quantified as $-0.0098 \pm 0.0005\ \mathrm{ppm/°C}$ [17]. The phase maps are represented as a single scalar value in a particular range, typically [-π, π], and because of this angles or phases outside of this range are wrapped around giving incorrect results. For example, rotations of π/2 and -3π/2 will both be given the value of π/2 after phase wrapping [18]. Phase unwrapping is thus needed to ensure the correct information is being retrieved from the acquired phase data. With accurate temperature mapping provided by MRI and the development of MRI compatible heating devices it is possible to monitor the temperature throughout the treatment in real-time. The accuracy of the above described PRF temperature mapping in an artifact free environment is around ±1°C [19]. The introduction of artifacts of various kinds will affect the accuracy of temperature measurements, resulting in unpredictable accuracy. The temperature information can be used in a number of ways to determine the extent of damage; the three methods will be described below. They are the temperature threshold technique, cumulative equivalent minutes at 43°C dose model (CEM$_{43}$), and the recently introduced improved cumulative equivalent minutes at 43°C dose model (iCEM$_{43}$).

2.1.2. Temperature Threshold

The temperature threshold technique of treatment monitoring and damage assessment is the simplest of the three described in this paper. A predefined temperature T_{crit} is used as an indicator for irreparable damage to tissues. This means that any region of tissue reaching a temperature of at least T_{crit} is deemed to be irreparably damaged or coagulated [20]. In clinical applications, maximum temperature maps are required to monitor the temperatures reached to determine if regions have reached t_{crit}. To acquire maximum temperature maps the maximum

values for all pixels over the duration of the heating is determined. The maximum temperature reached at a particular point can be expressed as:

$$T_{\text{max}} = \max_{t=0\ldots\tau}[T(t)]$$

2.2

where T_{max} is the maximum temperature at the point across all time and $\max[]$ is a function determining the maximum value of a set of numbers. When the following expression is true:

$$T_{\text{max}} \geq T_{\text{crit}}$$

2.3

the region in question is deemed irreparably damaged.

2.1.3. Cumulative Equivalent Minutes at 43°C (CEM$_{43}$) Thermal Dose Model

The CEM$_{43}$ thermal dose model is the most widely used dose model in thermal therapy and it is based on historical time-temperature relationships seen experimentally. It was first introduced by Sapareto and Dewey for use in hyperthermia procedures [21], but is currently being applied to the higher temperature coagulative thermal therapies as well. This model utilizes a reference temperature of 43°C, as experimental data showed a break at this temperature when looking at different time-temperature relationships yielding the same end point in terms of cell killing. This model assumes that a temperature increase of 1°C requires half the time for the same effect above 43°C and that below 43°C one quarter of the time is needed for the same cell killing effect for a temperature increase of one degree. This model can be better understood with a look at **Figure 2.1** as well as mathematically where the thermal dose is:

$$t_{43} = \int_0^\tau C^{(43-T(t))} dt \qquad C = \begin{cases} 0.25, T < 43°C \\ 0.50, T \geq 43°C \end{cases}$$

2.4

where t_{43} is thermal dose (equivalent minutes at °C), τ is the total heating time, and $T(t)$ is the temperature (°C) as a function of time [21].

It is also important to note that an ideal thermal dose model should have the same calculated dose value for a particular endpoint for any time-temperature combinations; this is also shown in **Figure 2.1**. As with the temperature threshold technique, a particular dose threshold value ($t_{43,\text{ crit}}$) must be used to determine the regions of damage. Similarly to the temperature threshold method when the following statement is true:

$$t_{43} \geq t_{43,\text{crit}}$$

2.5

for a region, that region is deemed to be irreparably damaged. The most widely used threshold value for the CEM_{43} thermal dose model is 240 equivalent minutes at 43°C [22], [23]. In other words, the target must be heated using a time-temperature combination, equating to the same damage that would be seen if the target was heated for 240 minutes at the temperature of 43°C, as described by the CEM_{43} model.
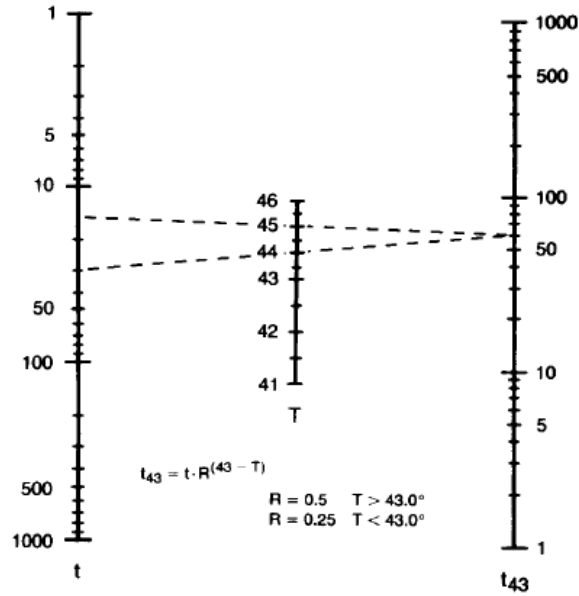
Figure 2.1: Two different time-temperature combinations will yield the same resulting thermal damage using the CEM_{43} thermal dose model. In both cases raising the target to the specified temperature for the corresponding length of time (15 minutes at 45°C and 30 minutes at 44°C) results in a dose equivalent to that achieved by 60 minutes of heating at 43°C. Reproduced from [24]

As stated previously, the CEM_{43} dose model was first introduced for use in hyperthermia treatments, which are performed at lower temperatures and longer exposure times as opposed to newer higher temperature coagulative thermal therapy procedures. The model was based on experimental results from lower temperature hyperthermia experiments being performed at the time. It comes with no surprise that with the higher temperatures now being used in coagulative thermal therapy procedures the CEM_{43} model no longer provides consistent and accurate dose predictions.
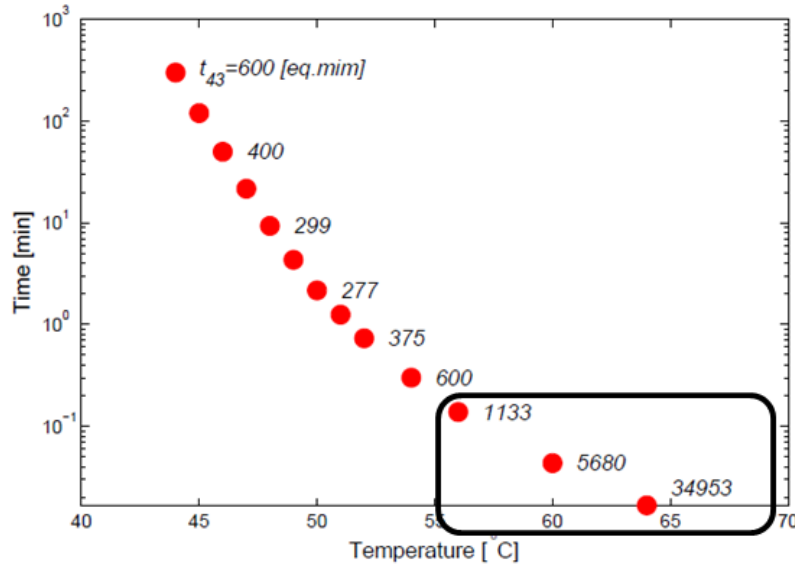
Figure 2.2: Time-temperature combinations by Henriques and Moritz which resulted in the same damage endpoint. Calculated CEM$_{43}$ dose values are also shown and in an ideal world should be equal [10].

As seen in **Figure 2.2** at the higher temperatures being used today (greater than 55°C) the CEM$_{43}$

dose model is no longer accurate in its damage prediction. All of the time-temperature

combinations shown in **Figure 2.2** are the results of an experiment performed on porcine skin.

These time-temperature combinations all resulted in the same biological effect and thus should

have the same calculated thermal dose. The experiment performed by Henriques and Moritz an

area of skin was immediately brought to a predetermined temperature and kept there and the

shortest required time for trans-epidermal necrosis (biological effect) was recorded for a variety

of different temperatures. The skin was brought to the temperature using a constant stream of

water at a particular temperature and the time needed to achieve the wanted trans-epidermal

necrosis was recorded [25]. These different durations and temperatures represent the different

data points in **Figure 2.2**. At the lower temperatures, for which the model was first introduced,

the calculated doses are fairly consistent, but as the temperatures increase this consistency is lost.

13

These discrepancies at high temperatures led to the introduction of a new thermal dose model, $iCEM_{43}$, first proposed by Hisham Assi [10].

2.1.4. Improved Equivalent Minutes at 43°C ($iCEM_{43}$)

As with Sapareto and Dewey's thermal dose model the $iCEM_{43}$ model also uses the equivalent minutes at 43°C metric for damage quantification. Again similarly to the CEM_{43} model, historical experimental data was fit, but this time to the modified Arrhenius equation known as the Vogel-Tamamann-Fulcher (VTF) equation. The VTF has been successfully applied to a number of different rate processes but, until Assi's work had never been applied to thermal dose applications [26], [27]. The VTF equation is expressed as:

$$\Omega = A \int_0^\tau e^{-\frac{a}{T(t) - T_0}} dt$$

2.6

where Ω is a specified amount of thermal damage, A (s^{-1}) is the frequency factor, a (°C) is a parameter related to the activation energy, and T_0 (°C) is the absolute temperature, below which the damage process can no longer be thermally activated.

Generalizing both the CEM_{43} and VTF based models to a form that expresses the thermal damage, D, as it depends on temperature both exponentially and cumulatively, gives rise to:

$$D = \alpha \int_0^\tau e^{\beta[T(t)]} dt$$

2.7

where $\alpha = A$ and $\beta[T(t)] = -\frac{a}{T(t) - T_0}$ for the VTF based model.

In a particular situation, that is a treatment at constant temperature over a length of time, equation **2.7** can be simplified and expressed as:

$$D = \alpha e^{\beta(T)}\tau.$$

<div align="right">2.8</div>

If at a particular temperature the damage seen is the same as that seen at a constant temperature of 43°C for time τ_{43} we are able to equate the two expressions for D and rearrange for t_{43} to find an equivalent minutes at 43°C equation written as:

$$\tau_{43} = e^{-\beta(43°C)}e^{\beta(T)}\tau.$$

<div align="right">2.9</div>

Now in order to apply this to a real-life situation it must be made into a form that allows for temperature which varies with time resulting in:

$$\tau_{43} = e^{-\beta(43°C)}\int_0^\tau e^{\beta[T(t)]}dt.$$

<div align="right">2.10</div>

Using equation **2.10** a relative time versus temperature relationship was then found and was used to find the constants for the iCEM$_{43}$ equation. These relationships for the CEM$_{43}$ and iCEM$_{43}$ models are,

$$\ln\left(\frac{\tau_{43}}{\tau}\right) = \begin{cases} 1.4T - 60°C, T < 43°C \\ 0.7T - 30°C, T \leq 43°C \end{cases}$$

<div align="right">2.11</div>

and

$$\ln\left(\frac{\tau_{43}}{\tau}\right) = \frac{a}{43°C - T_0}\frac{T - 43°C}{T - T_0}$$

<div align="right">2.12</div>

respectively.

To find the constants, Assi looked back at four different published data sets each providing exposure times at constant temperatures to achieve the same thermal damage end point for each experiment. These experiments were on different biological systems, three of them

<div align="center">15</div>

being cell survival studies [28–30], while the final one was irreversible epidermal damage of

porcine skin [31]. Using the relative time versus temperature relationships described above, the

data sets from the experiments were plotted along with the curve representing the CEM_{43} model.

Lastly the $iCEM_{43}$ curve was fit to the data to determine the values for the constants. This

analysis is best summarized in **Figure 2.3**, which shows the aforementioned plot of relative time

versus temperature with the models.
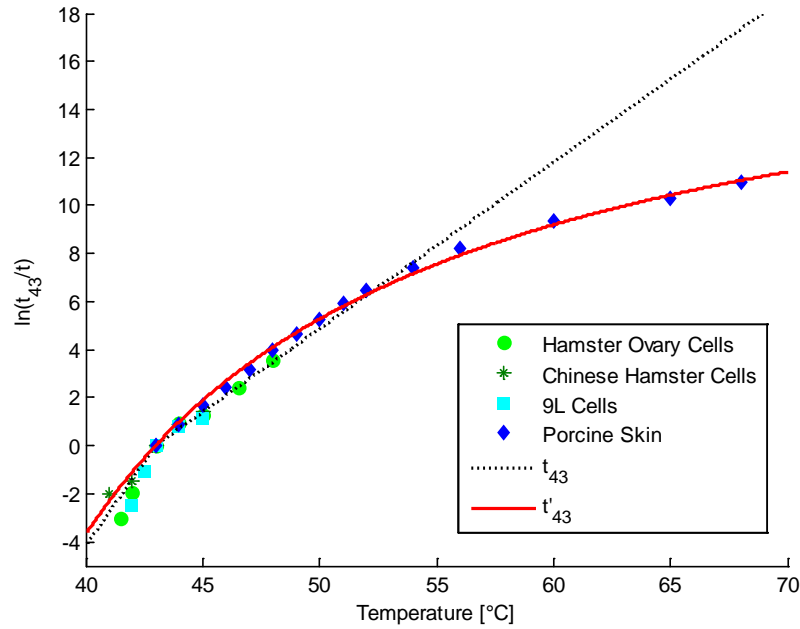
Figure 2.3: *Normalized time-temperature relationship for four different experimental data sets, as well as curves representing the CEM_{43} dose model and the for the $iCEM_{43}$. Adapted from* [10]. *Data taken from* [28] *for hamster ovary cells,* [29] *for Chinese hamster cells,* [30] *for 9L cells, and* [31] *for porcine skin.*

As stated previously, the CEM_{43} is a good fit at lower temperatures, however at the higher

temperatures, as seen in **Figure 2.3**, there is a drastic deviation between the data and the curve

representing the CEM_{43} model. On the other hand, the $iCEM_{43}$ model shows a good fit

throughout all temperature ranges, with the values for the constants being $\frac{a}{43°C-T_0} = 19.6$ and

$T_0 = 23.5°C$. The iCEM$_{43}$ thermal dose model can be expressed in a form similar to that of the CEM$_{43}$ as:

$$t'_{43} = \int_0^\tau (3.25 \times 10^8)^{\frac{T(t)-43°C}{T(t)-23.5°C}} dt \qquad \textbf{2.13}$$

where t'_{43} is the dose in equivalent minutes at 43°C. As with the previous two methods a threshold dose $(t'_{43,crit})$ is used to determine whether a region is irreparably damaged or not and when the below statement is true:

$$t'_{43} \geq t'_{43,\,crit} \qquad \textbf{2.14}$$

the region being analyzed is considered to be irreparably damaged. As discussed in **Section 1.3** Assi performed some preliminary experiments to compare the consistency of both the CEM$_{43}$ and iCEM$_{43}$ thermal dose models which yielded promising results, however further investigation is needed.

3. Materials and Methods

3.1. Overview

In order to further test the consistency of all three models, relevant clinical data from coagulative thermal therapy was required. With permission from Dr. John Trachtenberg at Princess Margaret Hospital, data from an ongoing clinical trial was provided to test the different dose models. The clinical trial from which the results of this thesis were produced was run under ethical guidelines with appropriate ethics board approval at the University Health Network. The data sets used in this thesis were provided completely anonymized, and it was not possible to link any data with a particular patient. The clinical trial is real-time MRI-guided focal laser therapy for the treatment of low risk prostate cancer [9]. The procedure has been evolving as the trial has progressed, however the end goal of treating a localized region of the prostate while minimizing damage to healthy tissues and minimizing unwanted side effects, remains the same. Despite this evolution the main components of the procedure remain unchanged. Firstly, the patient is under general anesthesia, one or more laser fibers are inserted free hand using a needle under MRI guidance, with a template, similar to that seen in the implantation of brachytherapy seeds. Saline-filled fiducials within the insertion template are seen in MRI scans, and used to ensure the needle is inserted in the proper location. Once in the correct location, the laser fiber is inserted and a part of the target is heated while MR thermometry maps are acquired every 6 seconds. The laser fiber(s) are then repositioned to heat another part and this repositioning and heating is repeated until the entire target region reaches the desired dose threshold. The duration of each heating fraction ranges from 4 to 10 minutes in length, and the laser power is in the 4 to 10 Watt range. The laser fibers are removed and finally a post-treatment gadolinium contrast

enhanced MRI (ptgMRI) is performed to view the damaged region. Gadolinium contrast agents are injected into the patient's bloodstream and due to its magnetic properties increases the signal in the regions where it is present. The areas where the gadolinium is present will show up as brighter regions on an MRI scan. Conversely, regions where the gadolinium is not present will have lower signal intensities and thus show up as darker. In the case of the procedure being described here, the region of damage is seen as the dark region where gadolinium is not present. This is the result of the vascular shutdown in the treated region, which stops the flow of blood containing the gadolinium contrasting agent. Vascular shutdown is destruction or loss of function of the blood vasculature in a particular region. In the case of coagulative thermal therapy the heat denatures important proteins in the cells and leads to tissue coagulation. This tissue coagulation disrupts the blood supply from the surrounding healthy tissues the treated region. The exact reason for this destruction of microvasculature in tumour cells is not well known but metabolic factors, decreases in pH, as well as decreased erythrocyte flexibility have been suggested [32]. It is for this reason that the damaged regions can be seen as dark regions on gadolinium contrast enhanced MRI scans.

3.2. Data Analysis

Data was provided for four patients. It consisted of MRI phase (temperature) and magnitude maps acquired every 6 seconds and ptgMRI images with overlaid damage contours. Image data from MRI scans is acquired as complex data sets, with a real and imaginary part. Depending on what one wants to look at this data is manipulated in different ways. Magnitude maps are the result of taking the absolute value of finding the magnitude of the real imaginary parts and represent the strength of proton oscillations. This strength is directly related to number of protons present and magnitude maps are used to maximize SNR (signal to noise ratio). The

damage contours which were provided were drawn by one of the investigators at the hospital following the acquisition of the ptgMRI, enclosing the region of low signal. **Figure 3.1** shows an example of the data provided, showing slice 2 from Patient A.
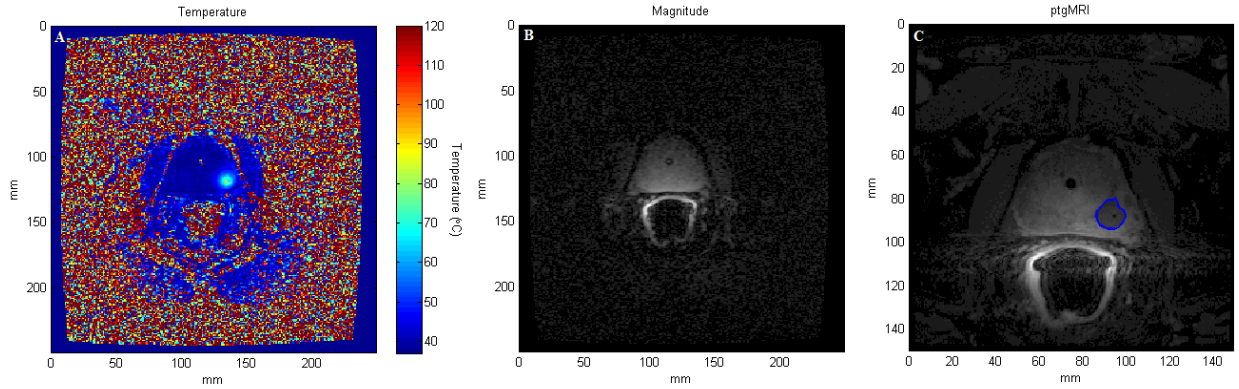
Figure 3.1: *Example of a data set for Patient A, Slice 2: (**A**) Temperature map at t = 3 mins, (**B**) Magnitude map at t = 3 mins, (**C**) ptgMRI with damage contour.*

With the provided data the goal was to calculate dose contour maps for each slice for both the CEM_{43} and $iCEM_{43}$ models and maximum temperature contour maps for the temperature threshold damage quantization method. For each slice, dose contours were calculated for both CEM_{43} and $iCEM_{43}$ dose models as well as maximum temperature contours, using the provided temperature history. The damage region seen in the ptgMRI was then compared to the calculated contour maps to determine a contour for each method that best described the region of damage. In other words, the aim was to find the answer to the following question: which dose and temperature contours best matches the one seen in the ptgMRI?

3.2.1. Co-Registering Temperature Maps and ptgMRI Scans

In some instances the slice location of temperature scans did not correspond to slice location of the available ptgMRI scans, which therefore could not be co-registered. For these cases interpolation could have been performed to allow for the two data sets to be in agreement,

but due to the time constraints of this thesis work, this was not done and these particular slices were discarded from analysis. In order to do the proposed analysis, it was required that the coinciding temperature maps and ptgMRI scans   be in the same coordinate system. Looking at **Figure 3.1** it is clear that this was not the case for the data provided. In order to co-register these two sets of images, simple scaling and 2-D translation was used on the temperature maps, to bring them into the coordinate system of the ptgMRI scan. A hybrid technique was used, where the scaling factor based on information stored in the scan files and the translation was determined via a landmarked-based minimization algorithm. Each type of scan had a different pixel size and the ratio of the two pixel sizes was used as the scaling factor. To determine the translation factors physical landmarks shared by the magnitude images and the ptgMRI scans were selected. After applying the scaling factor the translation factors in both the x and y directions were found.   The method to find these factors was to scan through different translation factors until the most suitable ones were found. By calculating the sum of the distances between the corresponding landmarks for each set of translation factors, the correct values were determined as the ones which resulted in the smallest sum of distances. This process was done on a slice-by-slice basis and **Figure 3.2** shows an example of the landmark selection and **Figure 3.3**, the results of the co-registration for Patient A, Slice 2.
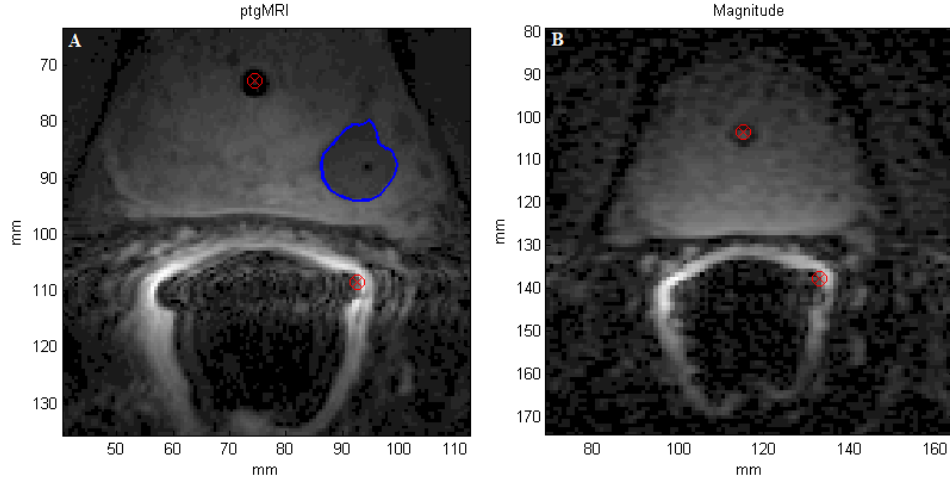
Figure 3.2: *Example of landmark placement on Patient A, Slice 2, (**A**) ptgMRI (**B**) Magnitude map at t = 3 mins.*
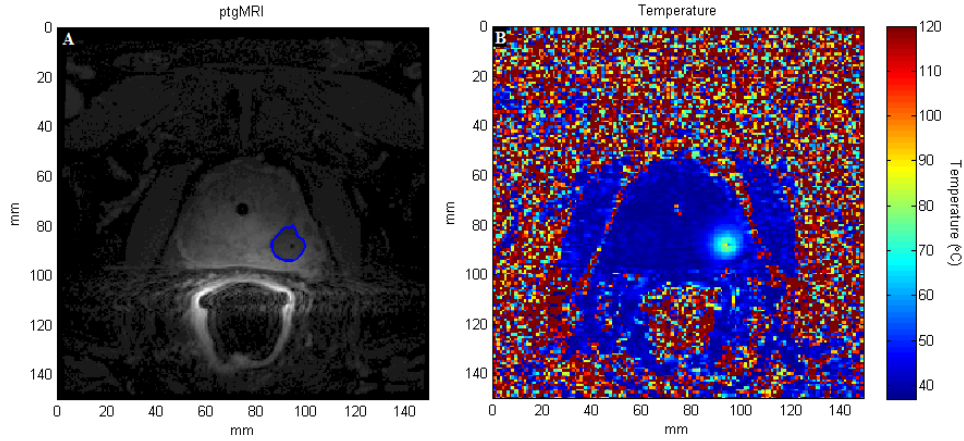
Figure 3.3: *Results of the co-registration for Patient A, Slice 2: (**A**) ptgMRI (**B**) Registered temperature map at t = 3 mins*

3.2.2. Dose Map Contouring and Best Contour Selection

As previously mentioned, the main goal of analysis was to find a threshold value for all three monitoring techniques. After the temperature maps were co-registered with the ptgMRI scans, due to the coarse nature of the provided temperature maps (128 pixels by 128 pixels), each temperature map was increased in size by a factor of 4 using bicubic interpolation to smoothen the data. Following this, full dose maps were calculated using the CEM_{43} and $iCEM_{43}$ dose models (equations **2.5** and **2.14**, respectively), as well as a maximum temperature map as

22

determined by using equation **2.6** over the entire heating time. An example of the results are shown in **Figure 3.4(A-B)** for the CEM_{43} and $iCEM_{43}$ dose map calculations and **Figure 3.4(C)** shows the maximum temperature map. When more than one heating fraction was performed at a particular slice, the accumulated dose from each fraction was added up to find the dose from the entire procedure. As with the accumulated dose maps, when more than one heating fraction was applied to a single slice, the overall maximum temperature for each pixel over all heating fractions was used to create the overall maximum temperature map.
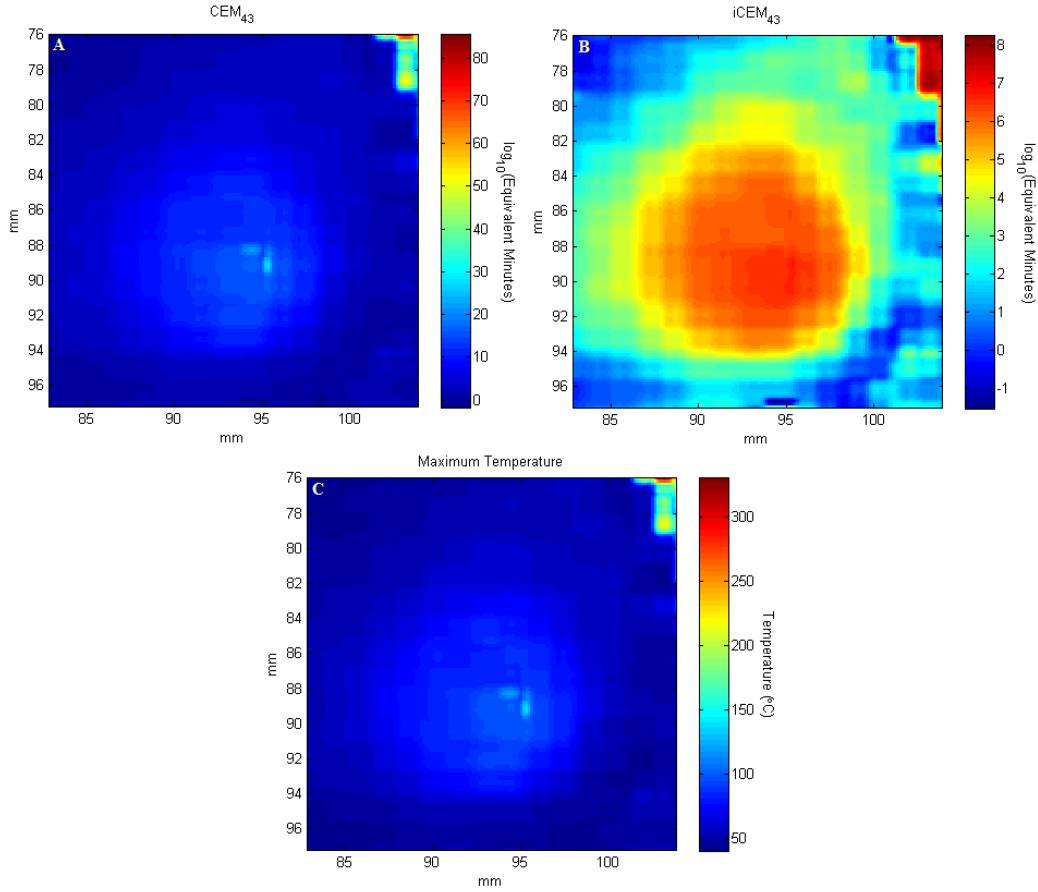
Figure 3.4: *Thermal dose and maximum temperature maps for Patient A, Slice 2 cropped to include only the area of heating for (**A**) CEM_{43} (**B**) $iCEM_{43}$, (**C**) Maximum temperature*

Following the calculation of the dose and maximum temperature maps, contouring of these maps was performed. The purpose of contouring these maps was to find the contour level

(threshold value) for each method and each slice that was the best match to the damaged region seen in the ptgMRI scan. Examples of this contouring can be seen in **Figure 3.5(A-C)** for the CEM$_{43}$, iCEM$_{43}$, and maximum temperature maps for Patient A, Slice 2. For illustration purposes, only 15 contour levels were chosen in these figures, for the actual analysis, 1000 contour levels were utilized for all three methods.

In order to determine which contour level (threshold dose) for each slice using all three models best represents the damage seen in the post-treatment scan a similarity metric was required. The Dice similarity coefficient (C_{DS}) has been used in similar studies, but mainly in the work of Yung et al. in their comparison of the temperature threshold method, CEM$_{43}$, and Arrhenius thermal dose models in canine brain tissue [33]. The C_{DS} can be calculated as:

$$C_{DS} = \frac{2|A \cap B|}{|A| + |B|}$$

3.1

where C_{DS} is the Dice similarity coefficient, A is the white pixels in the binary representation of the ptgMRI, and B is the white pixels after applying of thermal dose or maximum temperature thresholds.
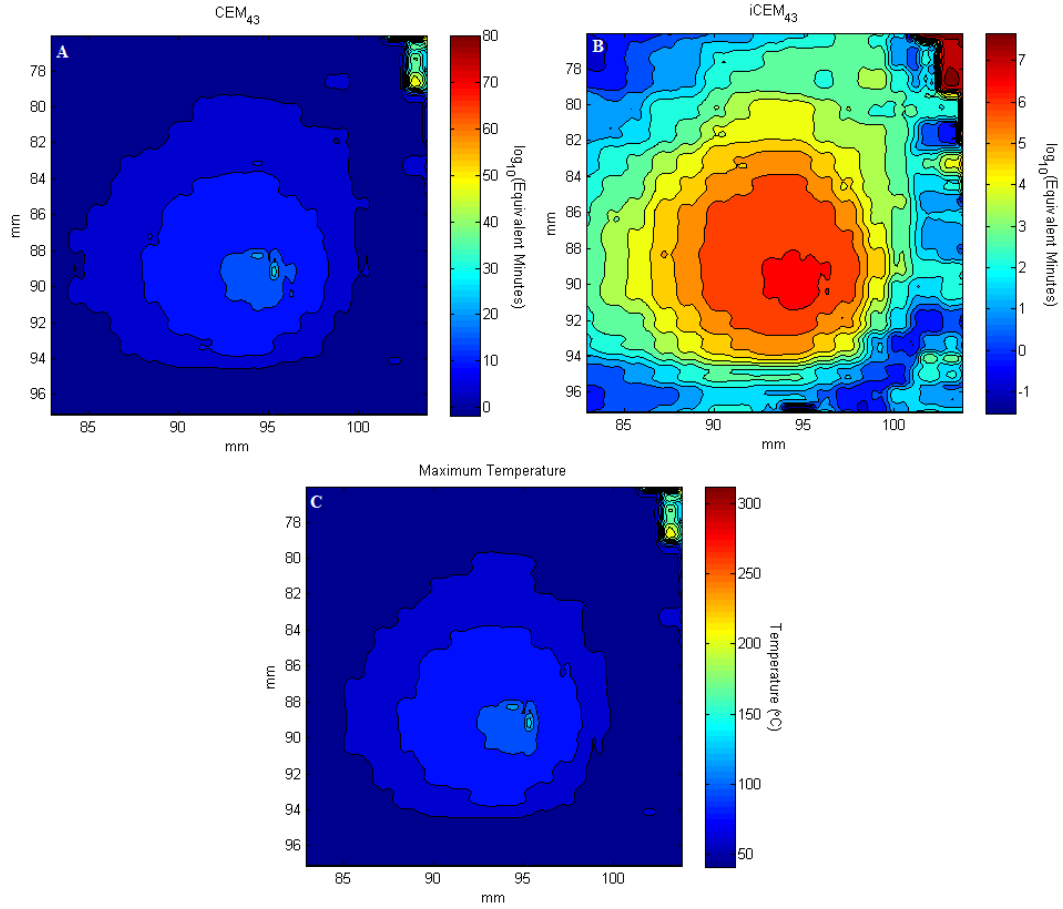
Figure 3.5: *Thermal dose and maximum temperature contour maps for Patient A, Slice 2 cropped to include only the area of heating for (**A**) CEM$_{43}$ (**B**) iCEM$_{43}$, (**C**) Maximum temperature*

To utilize the C_{DS} it was required that images be converted into binary images, that is a pixel values of 1 or 0. For each slice, an image of all black pixels was created, and the damage contour coordinates provided with the patient data from the researchers at Princess Margaret Hospital (**Figure 3.6(A)**) were flood-filled with white pixels to create a binary outline of the damaged area as shown in **Figure 3.6(B)**.
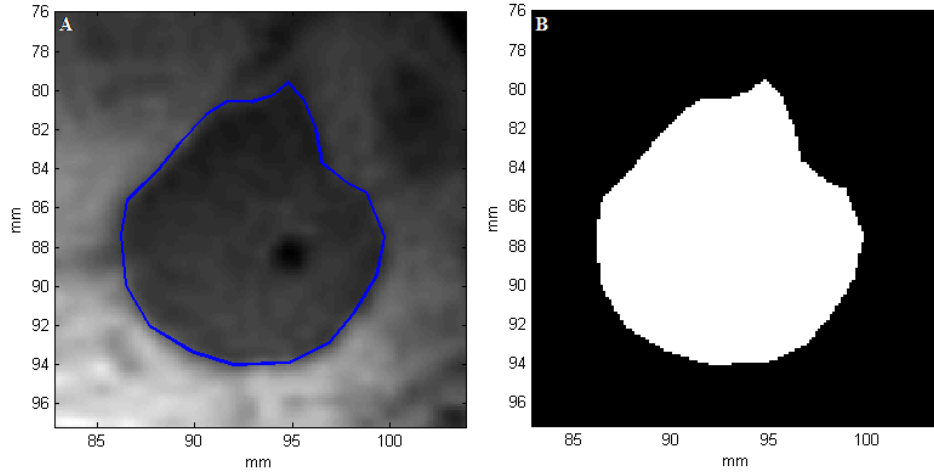
*Figure 3.6: Example of the conversion from greyscale ptgMRI scan with damage boundary (**A**) to binary representation of damaged region (**B**) for Patient A, Slice 2*

To establish which contour for each model best matches the region of damage, a similar binary image for each dose contour level (1000 per model) was created. For each contour the C_{DS} value was calculated against the damaged region, to evaluate the spatial overlap of the two regions. The contour level for each model that corresponded to the highest C_{DS} was taken as the threshold dose best representing the perfusion shutdown endpoint seen in the ptgMRI scans. **Figure 3.7** shows an example of the process of selecting the threshold dose corresponding to the highest spatial overlap, and thus best describes the dose that produced the measured outcome. This example uses the iCEM$_{43}$ thermal dose model and only 15 contour levels, and helps show the difference between predicted regions for each contour level. The images in **Figure 3.7** are of the best fitting threshold value results, as well as the ones both preceding and following it. This allows for the visualization of the progression along each contour level, and an understanding of how and why one threshold is considered the best fit. **Figure 3.7(C)** is the region that corresponds to the highest C_{DS} for all contour levels, and is thus selected as the threshold dose for the iCEM$_{43}$ for that particular patient and slice. As stated previously, for the actual analysis done for this investigation, 1000 contour levels were used as opposed to the 15 used here.
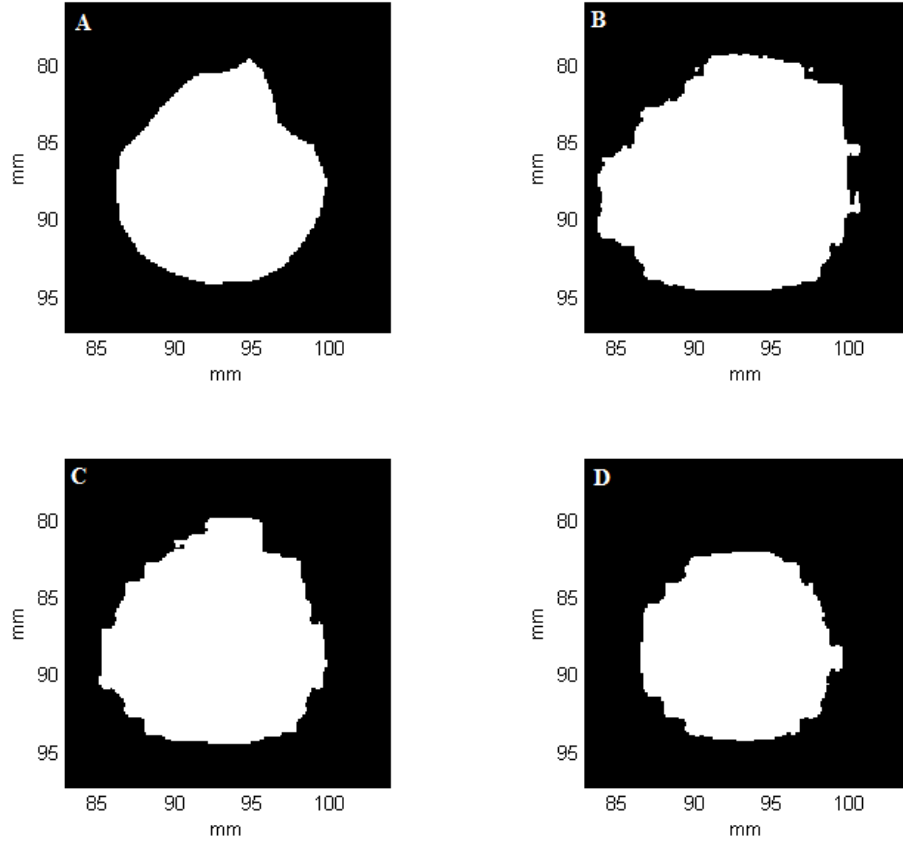
Figure 3.7: An example of the contour of best fit selection for the iCEM$_{43}$ Dose model for Patient A, Slice 2 using 15 contour levels where (C) is the selected best fit (maximum C_{DS} value). (A) The binary representation of the damaged region. (B) Predicted damage with smaller than ideal threshold dose, resulting in $C_{DS} = 0.8281$ (C) Predicted damage with ideal threshold dose resulting in $C_{DS} = 0.9208$ (D) Predicted damage with a larger than ideal threshold dose resulting in $C_{DS} = 0.9178$.

This analysis was then done for all slices of all patients for both the CEM$_{43}$ and iCEM$_{43}$ thermal dose models, as well as the temperature threshold method. **Figure 3.8** shows the contoured maps (15 contour levels) for all three methods, with the contour level garnering the highest C_{DS} for each method bolded.

27
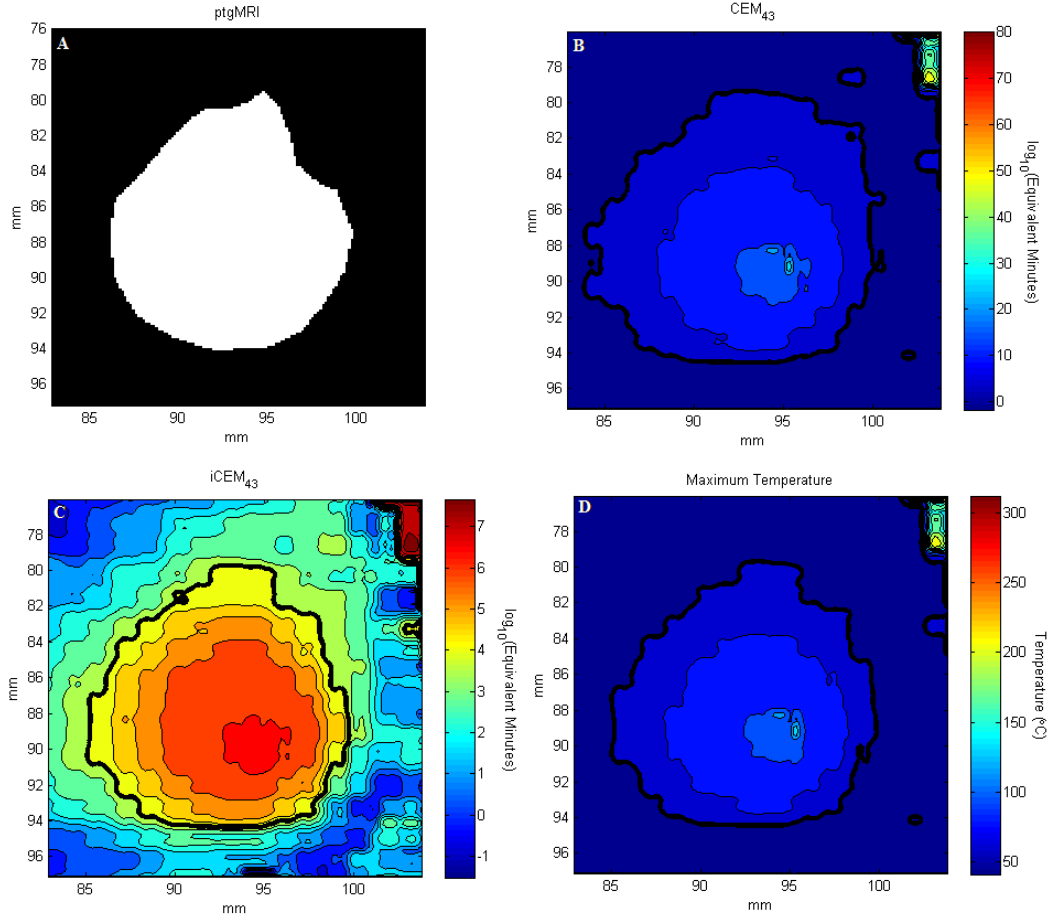
Figure 3.8: *Patient A, Slice 2, 15 contour levels with the contour of best fit bolded representing the area seen in (**A**) for CEM_{43} dose model (**B**) $iCEM_{43}$ dose model (**C**), and temperature threshold method (**D**).*

3.2.3. Artifact Determination and Remedies

Throughout the previously described process of analysis, artifacts of different kinds became evident when looking at some of the temperature maps that were provided. Some of these artifacts were simple in nature, and were easily remedied; others required a more detailed analysis into their cause and possible ways to eliminate or reduce them.

The first category of artifacts, the simpler one, was the result of inhomogeneities within the tissues and materials in the temperature scans. One particular case that was prevalent in a number of the slices being analyzed was the area of the urethra. Due to the insertion of a

catheter during the procedure, the information being received by the MRI in this area is not accurate, and thus can lead to incorrect temperature measurements. Another form of artifact that was seen was localized hotspots (random temperature spikes) away from the region of heating. To remedy these types of artifacts, the areas containing these issues were simply cropped out after applying the threshold to obtain the binary representation as seen in **Figure 3.9**. Areas that were distinctly separated from the actual heating region were simply cropped out on a slice by slice basis for each method separately.
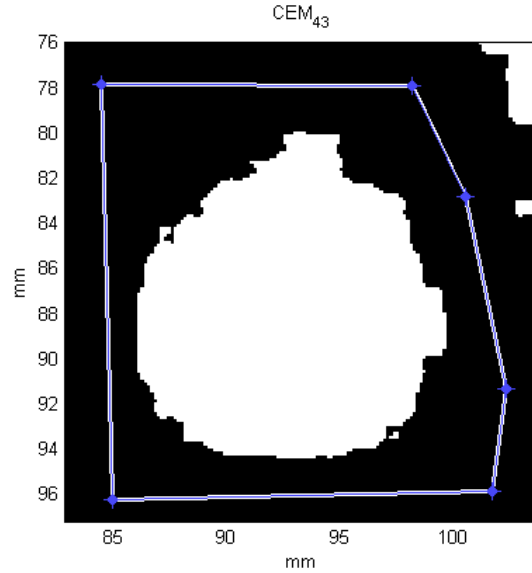
Figure 3.9: An example of a localized hotspot artifact away from the region of heating for Patient A, Slice 2, with the area cropped to remedy this issue also shown for the CEM₄₃ thermal dose model.

To do this, the maximum temperature map of the area of interest was used, and a free form area was drawn on the image to contain only the region of heating that is needed for analysis, and eliminating the localized hotspots. A binary matrix mask was created, where 1's were contained in the areas to be kept, and 0's in the areas to be eliminated. After applying the thresholds to the contour maps and prior to the C_{DS} determination, the threshold images were multiplied with this binary mask to eliminate any white pixels that would have been the result of these hotspots. This

was done in order to receive more accurate C_{DS} values, and was done to the threshold images, so that the actual contours would not be affected. A comparison of Patient A, Slice 1, results with this cropping done versus without cropping can be seen in **Figure 3.10** and **Figure 3.11** respectively. In this particular case you can see the white areas in the top right corner for the uncropped results, which results in a change in all of the calculate C_{DS} values. Although in this particular example the difference in C_{DS} values are not drastic, this was determined to be a necessary step to increase accuracy across all patients and slices.
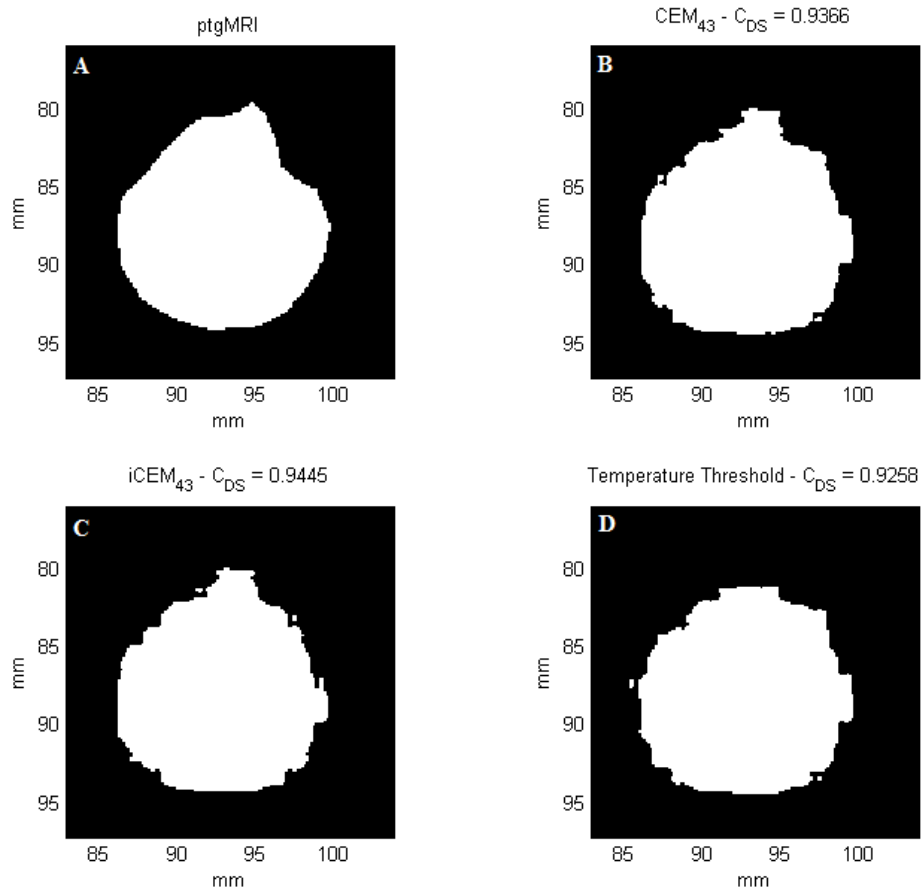
Figure 3.10: *Patient A, Slice 2 results following the cropping out of localized hotspots for (**B**) CEM$_{43}$ and (**C**) iCEM$_{43}$ thermal dose models and (**D**) the temperature threshold technique.*
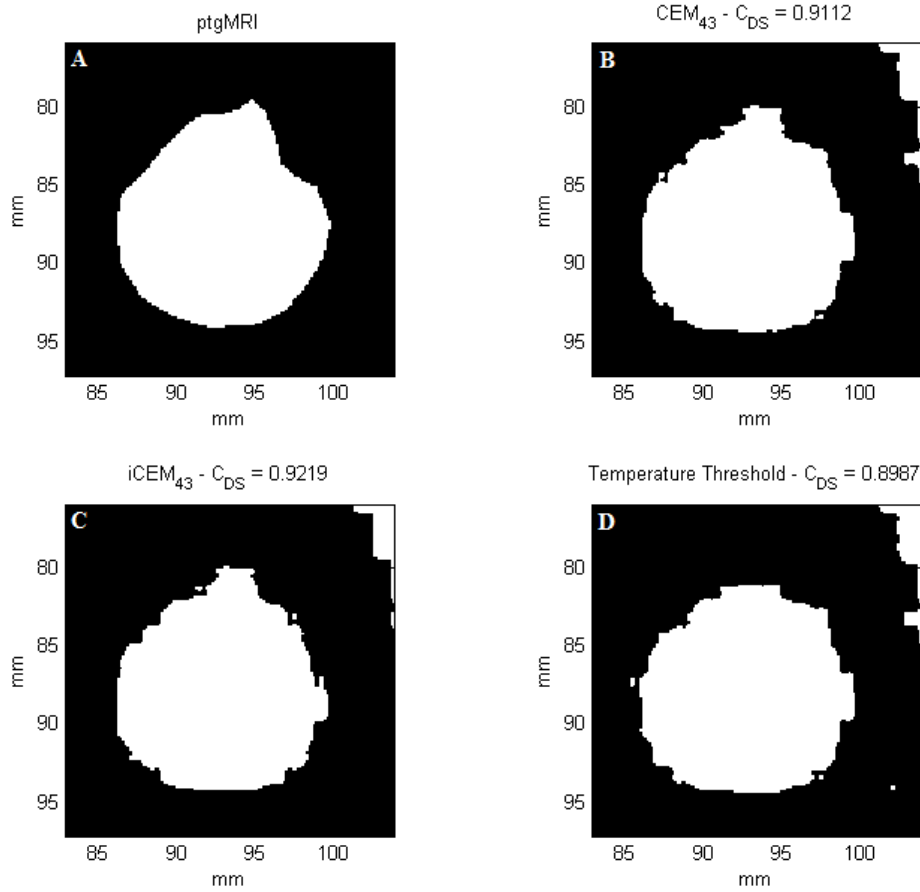
Figure 3.11: Patient A, Slice 2 results without cropping out of localized hotspots for (**B**) CEM$_{43}$ and (**C**) iCEM$_{43}$ thermal dose models and (**D**) the temperature threshold technique

Another more complex artifact was also discovered and MRI specialist, Dr. M. Sussman was consulted to garner further understanding. This type of artifact was the appearance of extremely high temperature pixel values near the center of the heating region, with adjacent pixels being an extremely low temperature value. Two of the provided patient data sets were severely affected by these types of artifacts and these cases were brought to Dr. Sussman to evaluate both the cause and potential solutions to these issues. Sussman is an Associate Researcher with the University Health Network, and the following information and conclusions were provided in a personal communication in the form of a report. First, a pixel was selected to determine if the temperature over time made physical sense. As seen in **Figure 3.12**, for the

31

particular pixel in question (132,125) the temperature versus time graph, on the right, from one

of the heating fractions for patient B, shows that the temperature information for this pixel is far

from accurate. After about 30 time steps, the temperature starts to plummet, and eventually

reaches improbably low temperatures (about -100°C), all the while the target is still being heated.
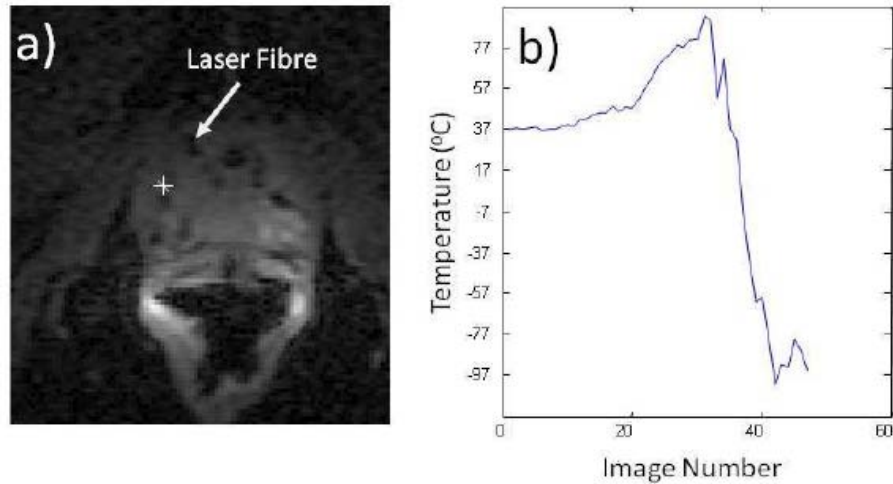
Figure 3.12: (A) Magnitude image from a patient with problematic data, with the asterisk highlighting a particular pixel (132,125). (B) Temperature history of the highlighted pixel from (A) [34].

To determine why this random temperature behaviour occurs, the data was looked at in greater

detail. In particular, as shown in **Figure 3.13** plots for the same selected pixel's (132,125) phase,

as well as its signal to noise ratio (SNR) were considered. In order to look at the SNR of the

given pixel, the noise for the entire image was first estimated and then the pixel value was

divided by the noise to obtain the SNR of the given pixel. To estimate the noise, the image was

broken up into small blocks and the standard deviation of image intensity within each of these

blocks was found. The lowest standard deviation of all of the blocks was taken to be the

estimate of the noise in the image. The reason that this is an estimate of the noise is that a block

containing only noise would have the smallest standard deviation, as any systematic error (not

noise) will result in an increase in the standard deviation.
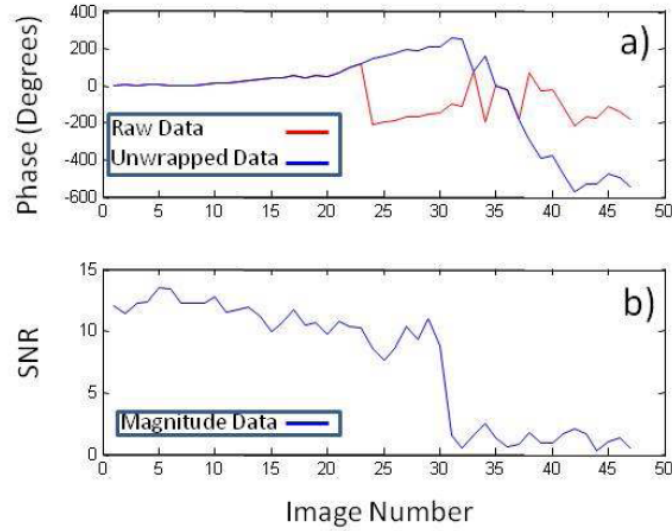
Figure 3.13: *(A) Phase data for the selected pixel from Figure 3.12, both raw data and unwrapped. (B) Calculated SNR (signal to noise ratio) for selected pixel* [34].

The unwrapped data is directly proportionate to the temperature change as can be seen if you compare this blue line, to the plot in **Figure 3.12(B)**. The first thing that may stand out is the drastic jump in the raw data (red line) at time step 21, which is attributed to phase wrapping and is thus remedied during the phase unwrapping procedure as seen in the blue line. As with the temperature history the unwrapped phase data begins to act in a very random nature at around time step 31. To look at why these random oscillations in temperature occur, the plot showing the SNR over time was looked at. As expected prior to time step 31 the SNR is of an acceptable level, however from time step 31 onwards the SNR drops to a drastically low value in the range of 1 to 2. At such a low level of SNR there is only a negligible amount of signal left in the tissue which means that the data we are acquiring is simply noise and not at all related to the temperature.

The next step was to try to determine what was causing this drop in SNR, which was drastically altering the data being acquired. The magnitude data for the entire heating duration for the heating fraction was then looked at slice by slice, concentrating on the area around slice

30, where this signal loss was seen on the selected pixel. It was found that after slice 30, a region of little to no tissue signal began to appear, and grow in size throughout the duration of the heating. This is in agreement with what is suggested by **Figure 3.13(B)** where starting at slice 31 the SNR dropped drastically, leaving only noise. There are a number of explanations for this type of signal loss region, namely, tissue necrosis, charring, and gas bubble formation. Both charring and tissue necrosis are seen on MRI scans due to the physical change in the tissue, and thus its relaxation parameters. These changes would thus result in signal loss regions remaining following the procedure as both necrosis and charring are irreversible. If the onset of signal loss was the result of gas bubble formation from the high temperatures being reached during the heating, the regions of signal loss would be temporary. To investigate whether the signal loss was temporary three more magnitude images were compared, the first and last slices from the same heating fraction (series 43), and the first slice from the next heating fraction (series 45). All three of these images can be seen in **Figure 3.14**, it is important to note, that all three of these images are of the same physical slice.

Figure 3.14: Comparing the first slice and last slices of series 43, with the first slice of the next series, to determine the cause of signal loss seen [34]*.*

Looking at **Figure 3.14** it is quite evident that the region of signal loss seen during the heating was in fact temporary, as the large region seen at the end of series 43, is not present in series 45.

As the result of this comparison it is fair to conclude that the signal loss region is most likely the result of gas bubble formation during heating.

This type of artifact has been seen before, as discussed in the work of Viallon et al. where temperature inaccuracies as large as 45°C in either the positive or negative direction were found as the result of bubble formation [35]. Unfortunately there is no remedy to the type of temperature inaccuracies presented by gas bubble formation. Thus the only logical next step was to screen the received patient data to determine if gas bubble formation was present during the procedure and if it interfered with the analysis. If the quality and accuracy of data was affected by gas bubble formation it was not considered for the analysis done for this investigation. An example of a screening procedure is shown in **Figure 3.15**, where the pixels who have calculated SNR was below 2 at this particular image in time was plotted red. Slices with a large number of these pixels (>3% of cropped region of interest at single time step) on more than 25% of time steps were eliminated and on one occasion an entire patient was eliminated for this reason.
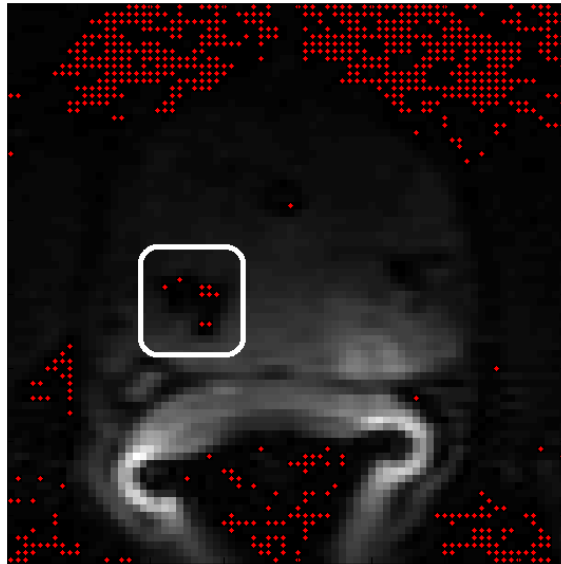
Figure 3.15: An example of the screening process for ruling out slices for thermal dose analysis where the red dots represent pixels with SNR values less than 2. The white box indicates the region of interest for this particular slice, as this is where the heating is taking place.

35

4. Results

4.1. Results Overview

In total, full data sets as described in **Chapter** 3 of this paper, were provided for a total of six patients undergoing Real-Time Magnetic Imaging-Guided Focal Laser Therapy for the treatment of lower risk prostate cancer. Each of these patients underwent slightly different procedures with respect to the number of laser heating locations, their duration, as well as the laser intensity. Of these provided six patients, only four of them were used in this investigation for two main reasons. The two patients that were ruled out were due to the inaccuracies in the temperature data provided, as discussed in the previous section. These two patients had temperature data that was severely affected by artifacts, both from gas bubble formation, as well as other sources, mainly tissue inhomogeneities, resulting in unusable data.

The results below represent four patients with different numbers of heating fractions, locations, and durations. Patient A underwent a single laser ablation in the prostate, and temperature mapping was performed across five 3mm thick slices. An example of the time-temperature history during the procedure at three different points for Patient A, Slice 2 can be seen in **Figure 4.1**
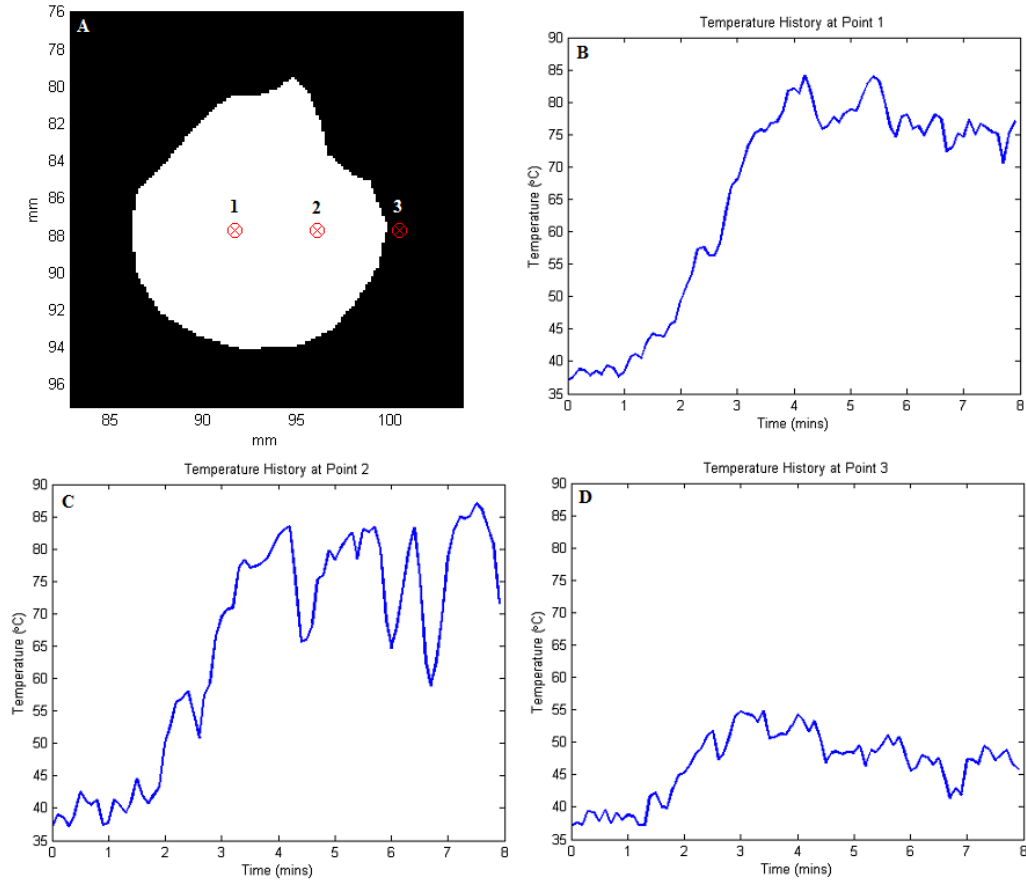
Figure 4.1: *An example of the temperature history for Patient A, Slice 2. (**A**) The ptgMRI with three points of interest shown. (**B-D**) The time temperature relationships at points 1-3 respectively.*

Patient B underwent 4 laser ablations in the prostate, with each ablation having temperature mapping across five 3mm thick slices. Patient C underwent 2 laser ablations, again with each one having temperature mapping across five 3mm thick slices. Lastly, for Patient D 5 laser ablations were performed in the prostate, again with temperature mapping performed across five 3mm thick slices for each heating fraction. An example of the time-temperature history for a multiple heating fraction procedure can be seen in **Figure 4.2**. This example shows the Time-temperature history at a given point for Patient D, Slice 5, for the 4 heating fractions that affected this particular slice.
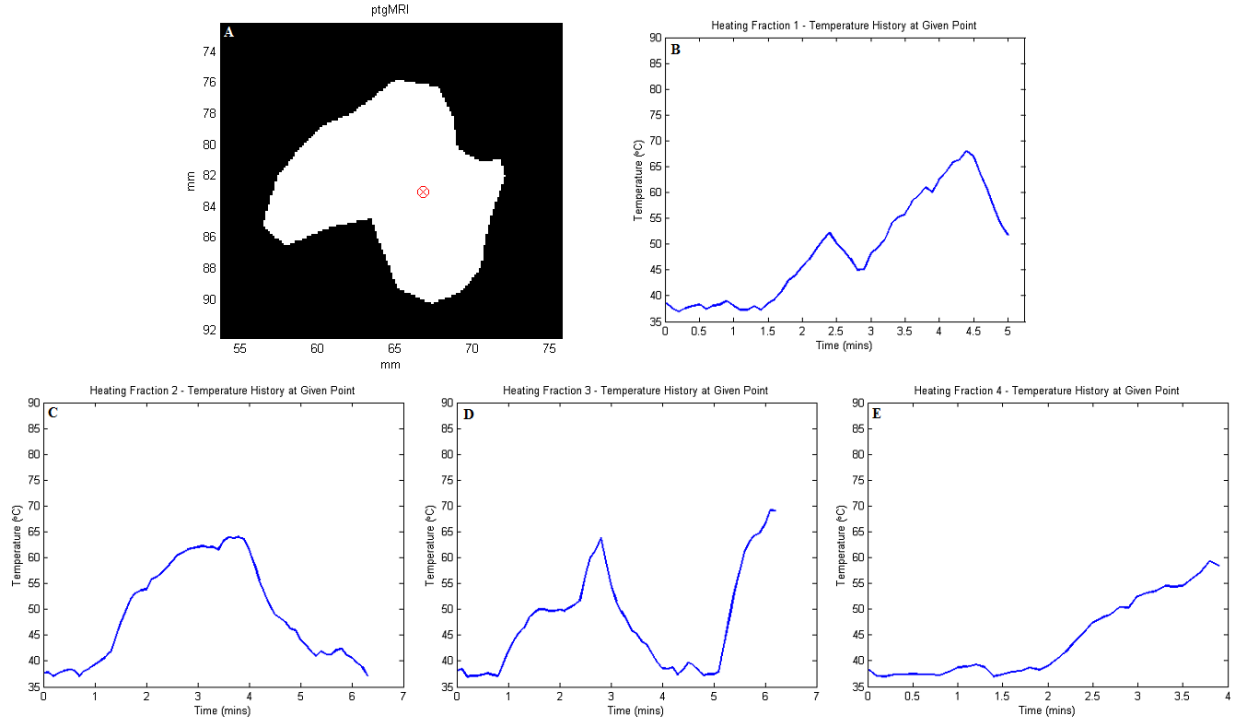
Figure 4.2: *An example of the temperature history for Patient D, Slice 5 at the point of interest shown in (A) The ptgMRI scan (B-E) The time temperature relationships at the point shown in (A) for the 4 heating fractions affecting this slice.*

4.1.1. Patient A Results

For patient A, five slices were analyzed as described in **Section 3.2** of this thesis. **Figure 4.3** below shows an example of the results for slice 2 for both the CEM_{43} and $iCEM_{43}$ thermal dose models, as well as the temperature threshold model.

Figure 4.3: Example results for Patient A, Slice 2. (A) The region of damage as seen in the ptgMRI scan. The region enclosed in the contour of best fit that best matches the region in (A) for (B) the CEM$_{43}$ model with $t_{43,crit} = 1.5270 \times 10^5 EM$, (C) the iCEM$_{43}$ model with $t'_{43,crit} = 1.9902 \times 10^4 EM$, and lastly (D) the temperature threshold technique with $T_{crit} = 60.67\ °C$.

It can be seen that all of the three methods of dose determination for this slice have a very good agreement with the damage seen in the ptgMRI scan. This can be seen both visually, as well as by looking at the calculated C_{DS} for each method, where they are 0.9362, 0.9446, and 0.9251 for the CEM$_{43}$ and iCEM$_{43}$ thermal dose models, and the temperature threshold technique respectively. For displays similar to **Figure 4.3** for all slices of Patient A, please consult **Appendix A**. In order to look at the consistency of all three methods, all slices were presented in a three bar graphs, and since all slices have the same end point (perfusion shutdown) the dose thresholds on a slice by slice basis should theoretically be the same. For patient A, **Figure**

39

4.4(A) represents the threshold dose using the CEM_{43} thermal dose model that had the largest C_{DS} (shown above each bar) for each individual slice. Similarly, **Figure 4.4(B-C)** display the threshold dose for the $iCEM_{43}$ thermal dose model and maximum temperature threshold respectively that yielded the highest C_{DS} for each slice. In order to better visualize variations between slices, the graphs for the CEM_{43} and $iCEM_{43}$ thermal dose models have been presented on a logarithmic scale.

Figure 4.4: Graphs summarizing the results for Patient A with the C_{DS} shown above each bar for (A) CEM_{43} dose thresholds, (B) $iCEM_{43}$ dose thresholds, and (C) Temperature thresholds

4.1.2. Patient B Results

For Patient B, a total of 4 individual laser heating fractions were performed in different locations, for varying durations. For each heating fraction, temperature maps were generated across 5 slices, with some slices being shared between the different heating fractions. The shared slices were determined via the use of the slice location information provided with the

MRI data. In total, damage was seen in 8 slices and analysis as described in **Section 3.2** of this thesis was performed on these slices. As with Patient A, an example of the results for a slice from Patient B, slice 5, is presented in **Figure 4.5**.
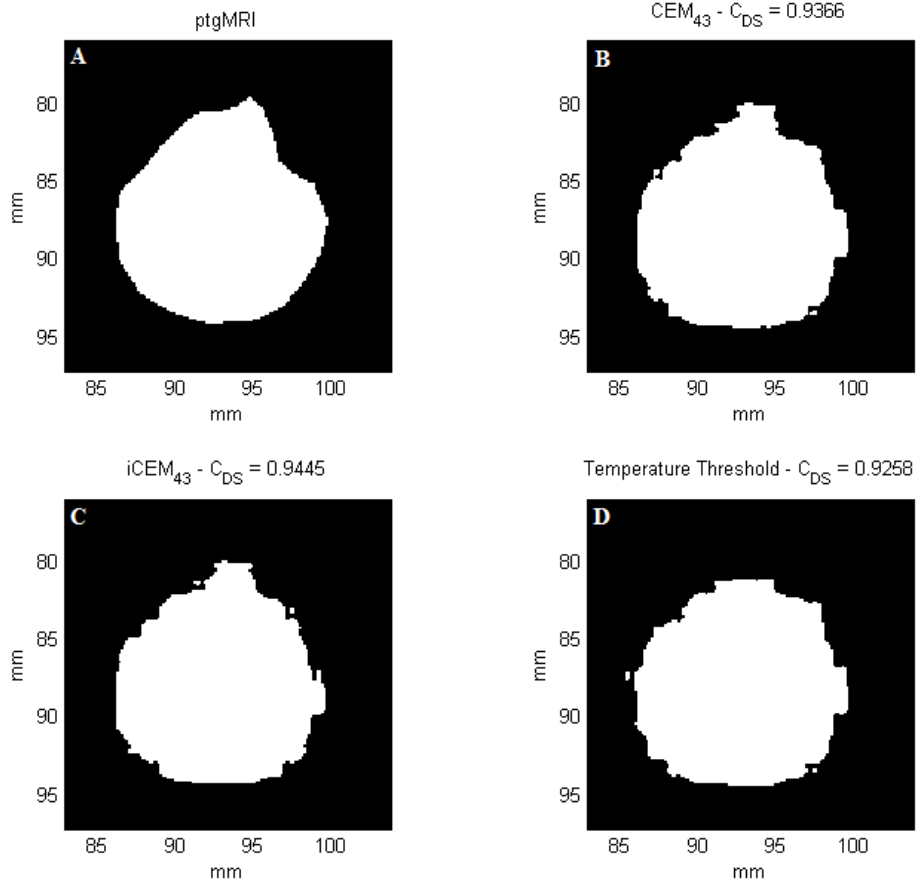

Figure 4.5: *Example results for Patient B, Slice 5. (**A**) The region of damage as seen in the ptgMRI scan. The region enclosed in the contour of best fit that best matches the region in (**A**) for (**B**) the CEM$_{43}$ model with $t_{43,crit} = 9.6720 \times 10^7 EM$, (**C**) the iCEM$_{43}$ model $t'_{43,crit} = 6.1861 \times 10^4$ EM, and lastly (**D**) the temperature threshold technique with $T_{crit} = 71.21\,°C$.*

As with the example shown for Patient A, all three methods of damage prediction are fairly consistent. This is evident by the calculated C_{DS} values of 0.8322, 0.8368, and 0.8294 for the CEM$_{43}$, iCEM$_{43}$, and temperature threshold methods. To see similar displays for all 8 slices from Patient B, please refer to **Appendix B**. For comparison of consistency all slices were presented together on three graphs, one for each of the CEM$_{43}$, iCEM$_{43}$, and temperature threshold methods. Firstly, **Figure 4.6(A)** shows the threshold dose for the CEM$_{43}$ thermal dose model for each slice, which garnered the highest

C_{DS} value when comparing it to the known damage area. **Figure 4.6(B)** shows the the thermal dose threshold for the iCEM$_{43}$ dose model, while **Figure 4.6(C)** shows the temperature threshold, the values for both of these methods was determined by finding the corresponding threshold values for the highest C_{DS} value for each slice.
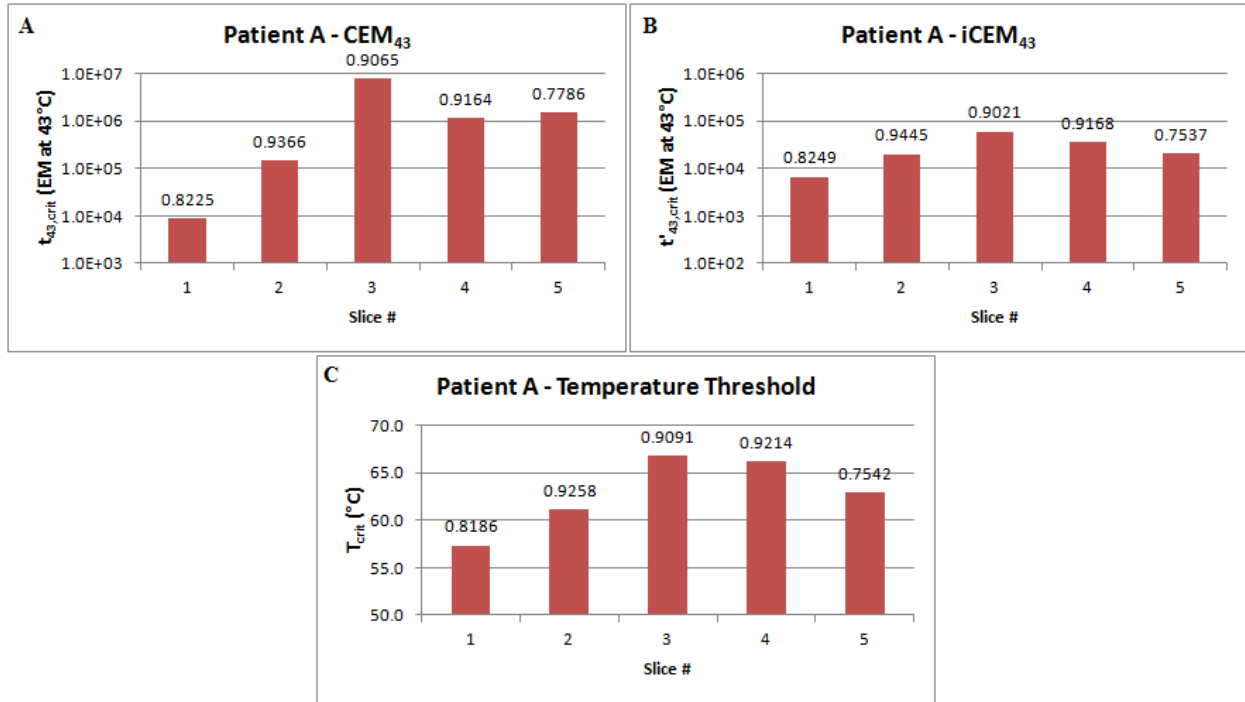

Figure 4.6: *Graphs summarizing the results for Patient B with the C_{DS} shown above each bar for (A) CEM$_{43}$ dose thresholds, (B) iCEM$_{43}$ dose thresholds, and (C) Temperature thresholds*

4.1.3. Patient C Results

Patient C consisted of 2 separate heating fractions, each with temperature mapping across five 3mm thick MRI slices. Of these 10 total slices of temperature information, only 4 slice locations were in agreement with slice locations of the ptgMRI scans. These four slices for which an agreement was seen were then analyzed as described in **Section 3.2**, to determine threshold values on a slice by slice basis for all three determination methods. As with the

previous two patients, an example of the results for Patient C for slice 3 is displayed in **Figure 4.7**. For a complete list of the results shown in the same format as **Figure 4.7** for all 4 slices that were analyzed for Patient C, please refer to **Appendix C**. Once again it is quite clear that all three methods do a similarly good job at matching the shape of the damage region, as indicated by the calculated C_{DS} values of 0.8629, 0.8670, and 0.8743, for the CEM_{43}, $iCEM_{43}$, and temperature threshold techniques.
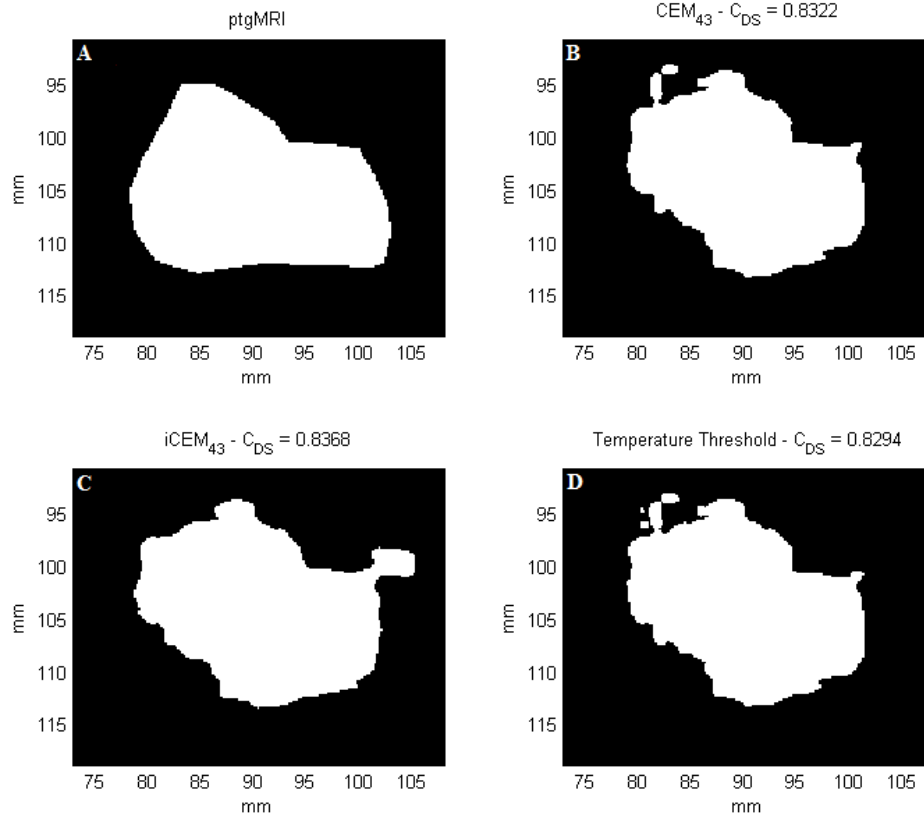

***Figure 4.7:** Example results for Patient C, Slice 3. (**A**) The region of damage as seen in the ptgMRI scan. The region enclosed in the contour of best fit that best matches the region in (**A**) for (**B**) the CEM_{43} model with $t_{43,crit} = 1.9142 \times 10^4$ EM, (**C**) the $iCEM_{43}$ model with $t'_{43,crit} = 4.8611 \times 10^3$ EM, and lastly the (**D**) temperature threshold technique with $T_{crit} = 54.09\,°C$.*

In order to visually compare the consistency on a slice by slice basis three graphs were produced, one for each method. **Figure 4.8(A)** shows the threshold dose that yielded the highest C_{DS} for each slice using the CEM_{43} thermal dose model, presented on a logarithmic scale.

Subsequently, **Figure 4.8(B)** is a similar graph for the iCEM$_{43}$ thermal dose model, again on the logarithmic scale. Lastly, **Figure 4.8(C)** shows the results on a slice by slice basis for the temperature threshold method.
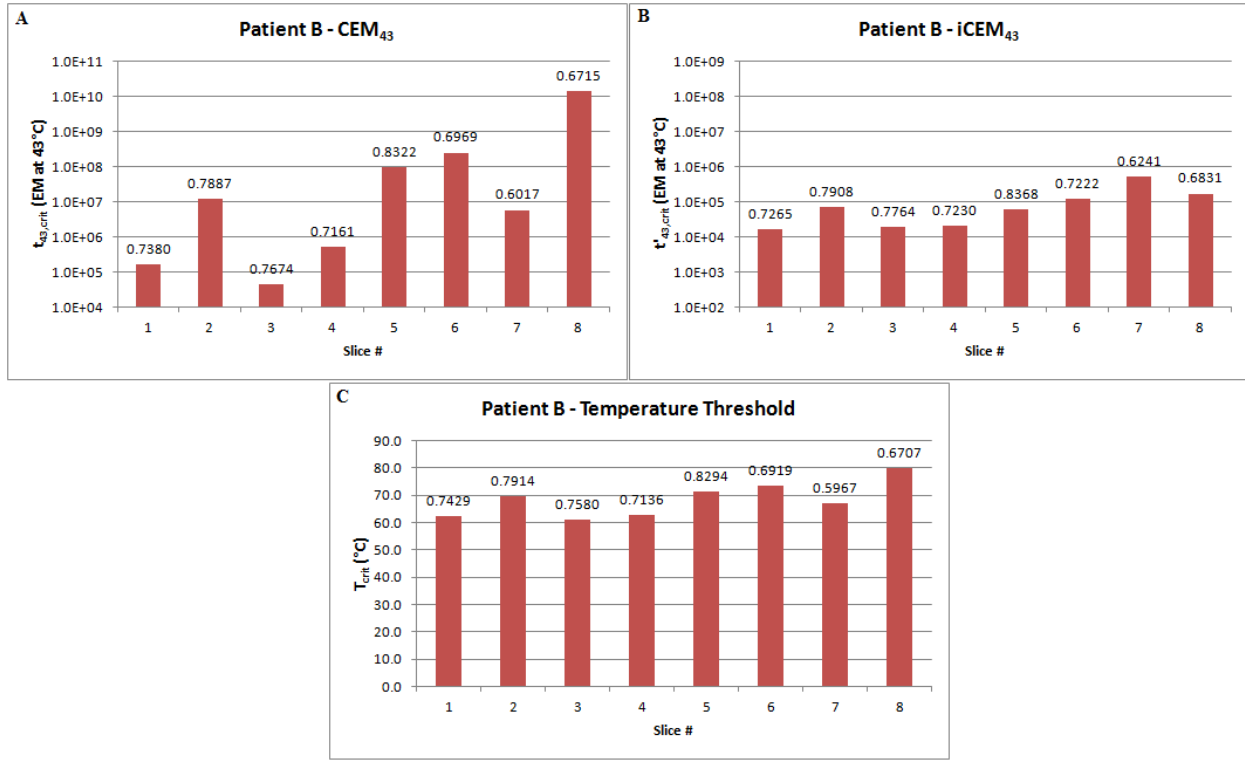

Figure 4.8: *Graphs summarizing the results for Patient C with the C_{DS} shown above each bar for (A) CEM$_{43}$ dose thresholds, (B) iCEM$_{43}$ dose thresholds, and (C) Temperature thresholds*

4.1.4. Patient D Results

The procedure for Patient D consisted of 5 separate heating fractions and as with all other patients temperature mapping was performed across five 3mm thick slices for each heating fraction, with some locations overlapping between fractions. In total 8 slices were analyzed as described in **Section 3.2**, and an example of the results for Patient D, slice 4 is provided in **Figure 4.9**. Once again all three methods produce consistent results in terms of producing a shape similar to that of the damage seen. This is evident by looking at the C_{DS} values calculated for all three methods, 0.8715, 0.8941, and 0.8568 for the CEM$_{43}$, iCEM$_{43}$, and temperature

threshold techniques respectively. Results presented in the same manner as **Figure 4.9** for all 8

slices for Patient D can be found in **Appendix D**. As with the previous 3 patients presented,

graphs displaying the threshold dose for each of the methods were generated. **Figure 4.10(A-C)**

shows the results for the CEM$_{43}$ and iCEM$_{43}$ thermal dose models, and lastly the temperature

threshold technique.
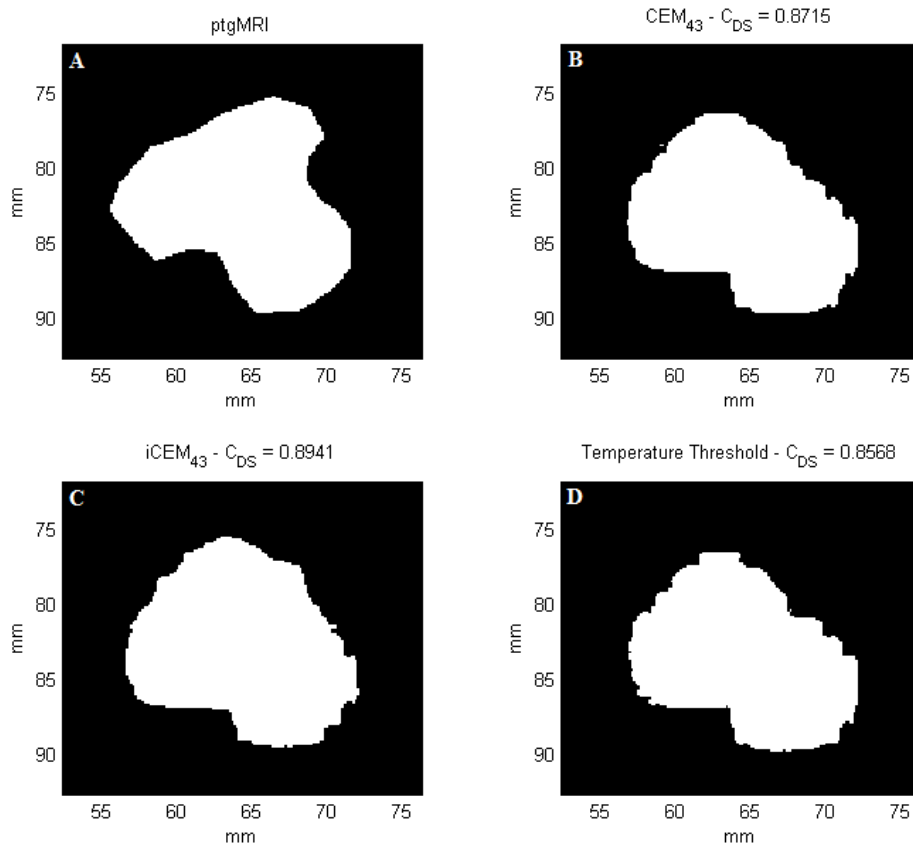
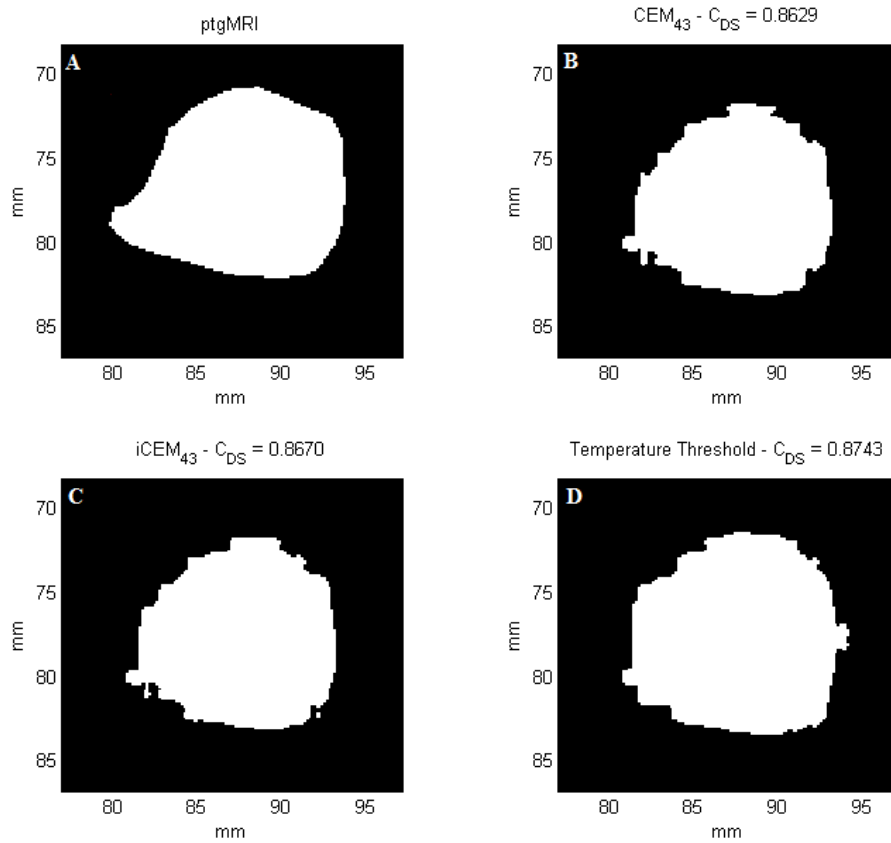***Figure 4.9:*** *Example results for Patient D, Slice 4. (**A**) The region of damage as seen in the ptgMRI scan. The region enclosed in the contour of best fit that best matches the region in (**A**) for (**B**) the CEM$_{43}$ model with $t_{43,crit} = 1.7157 \times 10^6$ EM, (**C**) the iCEM$_{43}$ model with $t'_{43,crit} = 2.6078 \times 10^4$ EM, and lastly (**D**) the temperature threshold technique with $T_{crit} = 66.06\,°C$.*
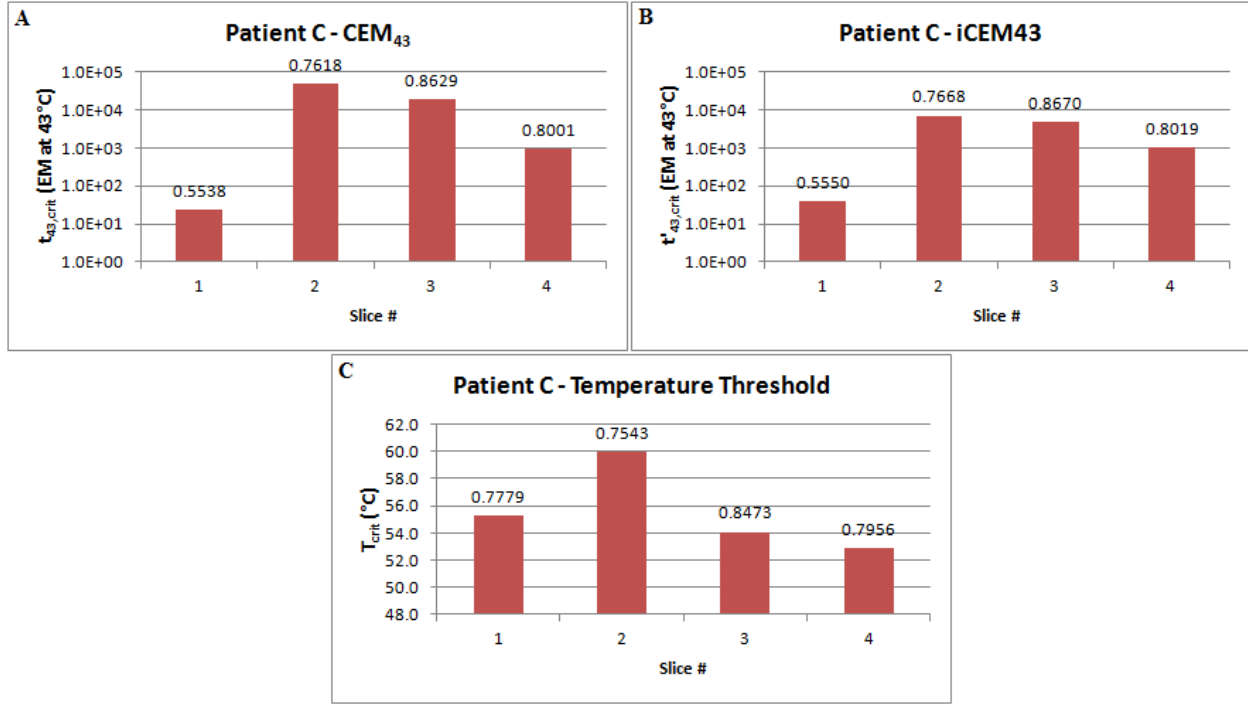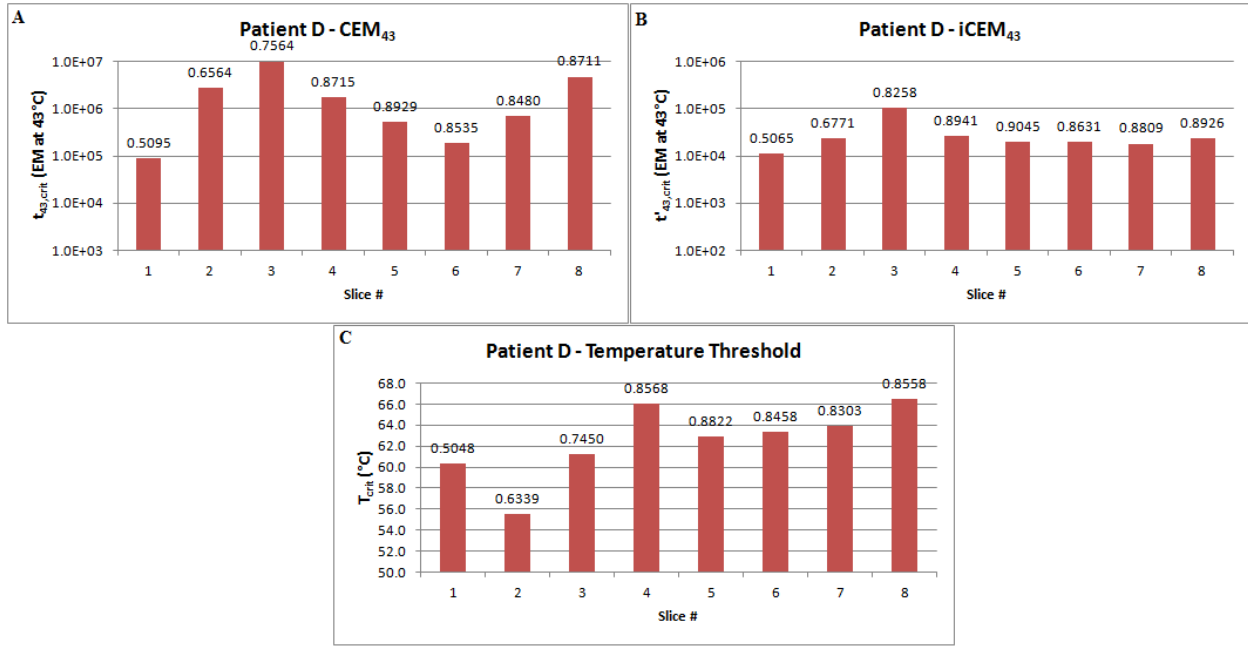
Figure 4.10: Graphs summarizing the results for Patient D with the C_{DS} shown above each bar for (A) CEM$_{43}$ dose thresholds, (B) iCEM$_{43}$ dose thresholds, and (C) Temperature thresholds

4.2. Compiled Results

Looking at all of the results for all of the patients it is important to note that some of the slices that were analyzed had very low C_{DS} values. The reasoning for these poor spatial correlations was mostly the result of temperature hotspots away from the main heating region, which were unable to be cropped out as described in **Section 3.2.3**. These hotspots would blend into the actual heating region, and thus the cropping was not possible without affecting the actual shape of the contour of best fit. **Figure 4.11** shows an example of this issue with Patient B, slice 4, where after applying dose and temperature thresholds, the area of damage is severely affected by the hotspots present in the top right and bottom left corners. It is clear that this particular slice does not have as high of a level of spatial correlation, as seen in the previous examples. This is evident by the low calculated C_{DS} values of 0.7084, 0.7172, and 0.7098 for the CEM$_{43}$, iCEM$_{43}$,

and temperature threshold techniques respectively. After looking at the results for all slices, it was decided that a criteria should be used to select only cases with an acceptable level of spatial correlation and avoid the inclusion of cases such as the one shown in **Figure 4.11**.
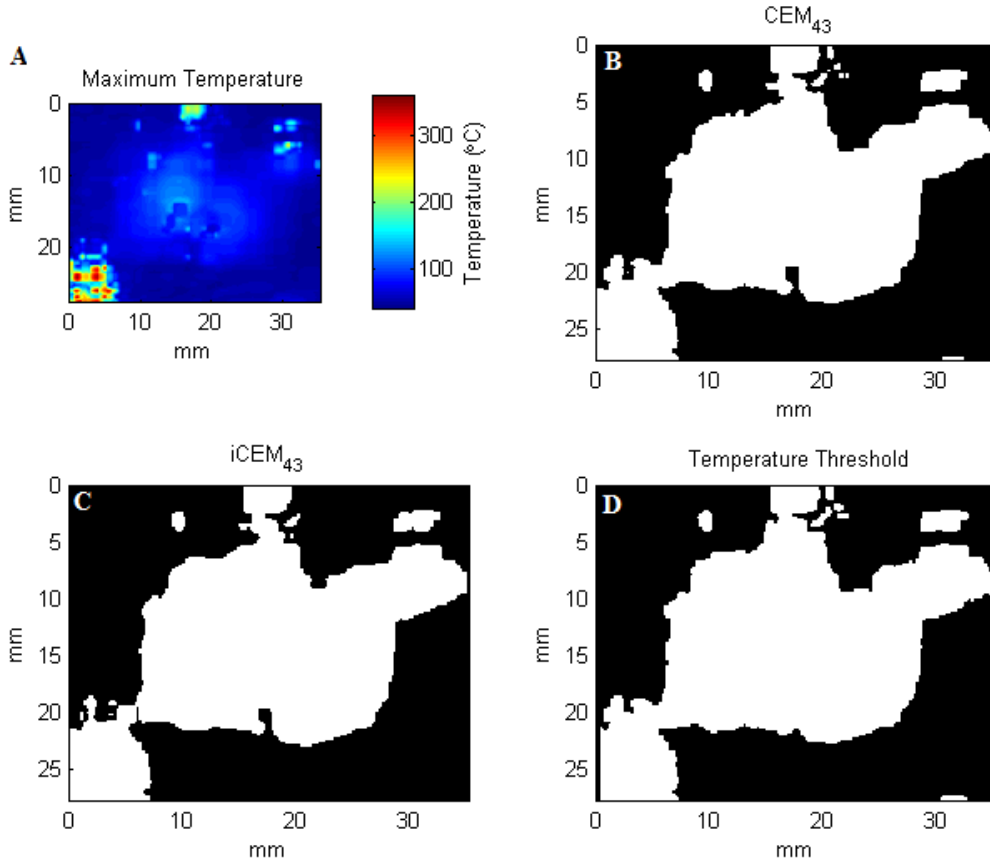
Figure 4.11: *Example of issues with hotspot artifacts away from heating region, affecting the threshold application and being unresolvable, leading to low spatial correlaton as indicated by C_{DS} values. (**A**) Maximum temperature map showing the hotspots that have blended in with central heating. (**B-C**) the regions of highest spatial correlation with their corresponding C_{DS} values for CEM_{43}, $iCEM_{43}$, and temperature threshold techniques respectively.*

Like in the previous example, some artifacts cannot be avoided and by using the C_{DS}, only slices without these issues would be used. Slices affected by these artifacts were found to have $C_{DS} < 0.8$, therefore only slices where $C_{DS} \geq 0.8$ were used.

The selected cases were then compiled into bar graphs, with all of the wanted slices from all of the patients on the same axis. **Figure 4.12(A-C)** shows the compiled results for the

CEM$_{43}$, iCEM$_{43}$, and temperature threshold techniques respectively. All of the results in **Figure 4.12** are shown in a form normalized dose (CEM$_{43}$ and iCEM$_{43}$) or normalized temperature rise (temperature threshold technique). In order to quantitatively compare the consistency of each method, a measurement metric was required, by normalizing both the thermal dose results (t_{43}, t'_{43}), and the temperature threshold results (T_{crit}), the standard deviation, σ, would be this measurement metric. By normalizing the results, it eliminates the dependence on the mean value and its units. For the CEM$_{43}$ thermal dose model the normalized dose (D_{43}) is expressed as:

$$D_{43} = \frac{t_{43}}{\langle t_{43} \rangle}$$

4.1

and for the iCEM$_{43}$ thermal dose model the normalized dose (D'_{43}) is:

$$D'_{43} = \frac{t'_{43}}{\langle t'_{43} \rangle}.$$

4.2

Lastly, to eliminate the dependence on the unit of measure for the temperature threshold technique, temperature rise

$$\Delta T = T_{\text{crit}} - 37°C$$

4.3

was used as opposed to the absolute temperature. The normalized temperature rise (ΔT_N) is then expressed as:

$$\Delta T_{\text{N}} = \frac{\Delta T}{\langle \Delta T \rangle}.$$

4.4

For all of the above equations the average values are found using all of the selected 11 slices, and then each threshold value for each slice is divided by this average for all three methods.

48
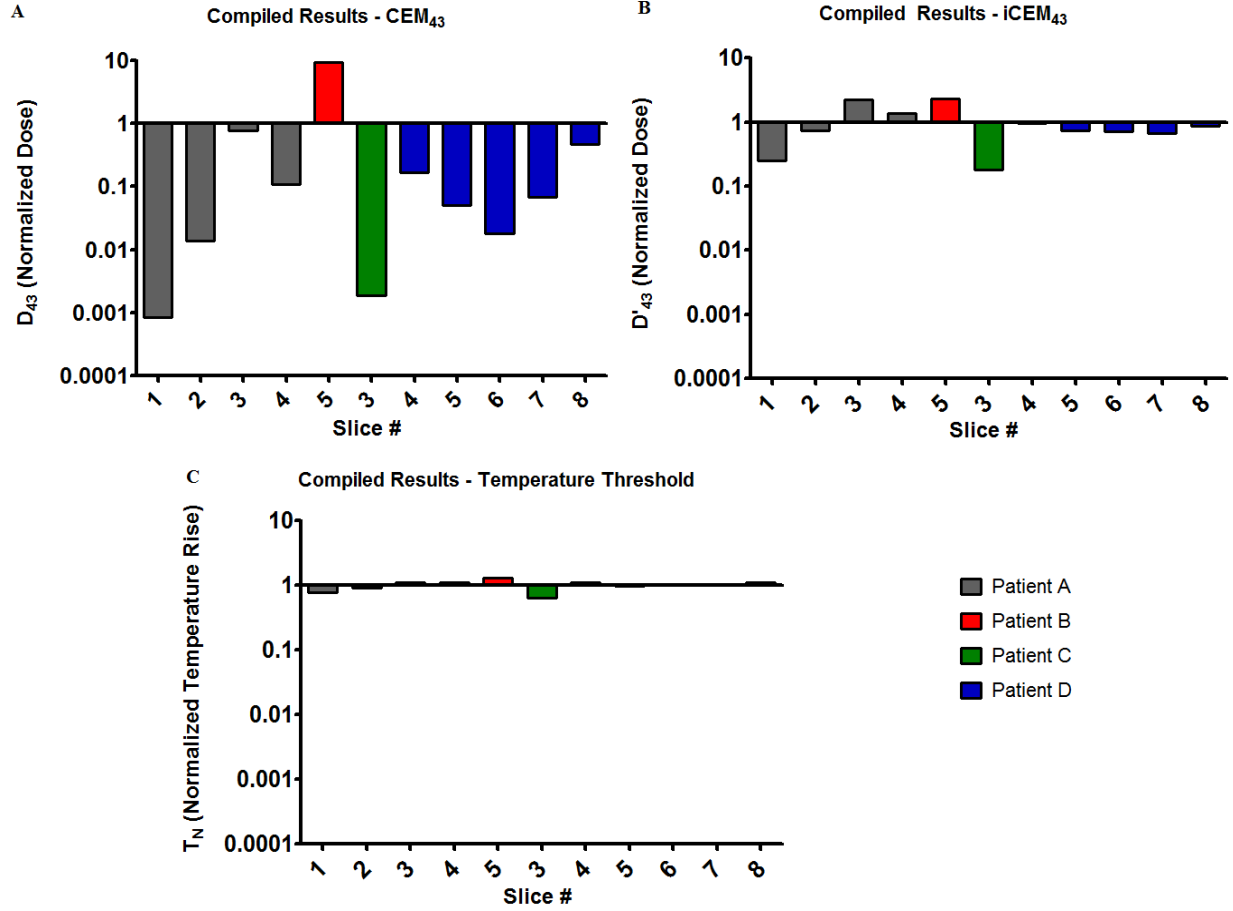
Figure 4.12: *Summary of results of only selected cases ($C_{DS} \geq 0.8$) for (A) CEM_{43} and (B) $iCEM_{43}$ thermal dose models and (C) temperature threshold technique.*

It is quite evident looking at the three graphs that there is a clear qualitative difference with respect to the consistency of their dose predictions. The calculation of σ was then performed for each method using the normalized values of only the slices selected in accordance to the C_{DS} value selection criterion as described previously (≥ 0.8). The normalized doses and temperature rises and their resulting σ values for each slice have been compiled in **Table 4.1**. It is quite clear by looking at the σ values (0.700 versus 2.78) that the $iCEM_{43}$ thermal dose model is much more consistent at predicting the threshold dose for the perfusion shutdown compared to the CEM_{43}

model. The temperature threshold σ value is even better, but this is expected with the type of procedure being used and this will be elaborated on in **Section** 5 of this thesis.

Table 4.1: Compilation of all slices that met selection criteria, with calculated normalized dose for CEM$_{43}$, iCEM$_{43}$, and the normalized temperature rise for the temperature threshold method. For analysis purposes σ was calculated and is also included in this table.

Patient	Slice #	D_{43}	D'_{43}	ΔT_{N}
A	1	8.4472×10^{-4}	2.4723×10^{-1}	7.6567×10^{-1}
	2	1.3924×10^{-2}	7.4256×10^{-1}	9.0815×10^{-1}
	3	7.6442×10^{-1}	2.2382	1.1195
	4	1.0865×10^{-1}	1.3512	1.0977
B	5	9.3437	2.2901	1.2872
C	3	1.8492×10^{-3}	1.7996×10^{-1}	6.4312×10^{-1}
D	4	1.6575×10^{-1}	9.6541×10^{-1}	1.0934
	5	5.0677×10^{-2}	7.3636×10^{-1}	9.7391×10^{-1}
	6	1.7673×10^{-2}	7.1915×10^{-1}	9.9209×10^{-1}
	7	6.7688×10^{-2}	6.6793×10^{-1}	1.0112
	8	4.6067×10^{-1}	8.6186×10^{-1}	1.1080
μ		1	1	1
σ		2.78	0.700	0.178

In addition to the calculation of the σ values for the normalized results for all three methods, the consistency of the three different methods was explored further. Using the calculated average dose threshold values used for the normalization seen in **Table 4.1**, each slice was revisited and a region of damage was predicted for the CEM$_{43}$, iCEM$_{43}$, and temperature threshold methods using these average values. The calculated average dose threshold values were 1.0347×10^7 EM and 2.7013×10^4 EM for the CEM$_{43}$ and iCEM$_{43}$ dose models

respectively, and the average T_{crit} was 63.58°C for the temperature threshold technique. To compare consistency, following the region formation using the average values, the C_{DS} was found for each slice and each method, **Table 4.2**. An example of this test for Patient A, Slice 2 can be seen in **Figure 4.13**. Comparing these C_{DS} values both individually and as a whole (normalized C_{DS} (N_{DS}) and σ_a), for each method would allow for a quantitative comparison with the method producing the smallest σ_a being deemed most consistent.
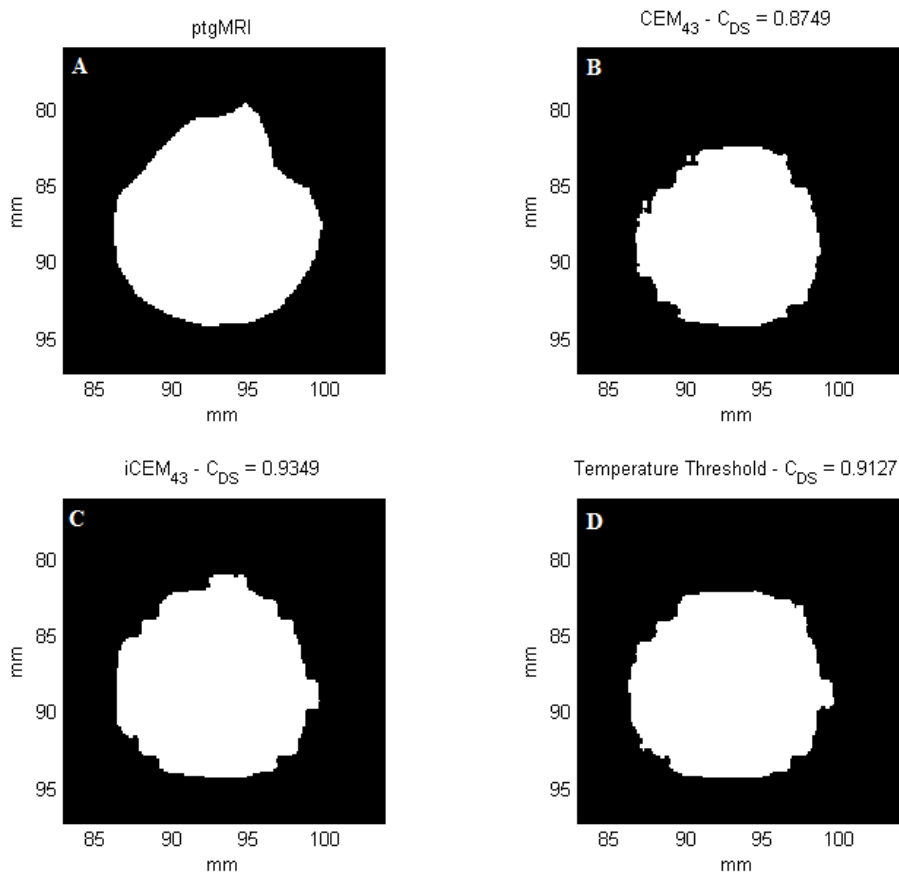

Figure 4.13: *Example showing the results of using the calculated average threshold values of $t_{43,crit} = 1.0347 \times 10^7$ EM and $t'_{43,crit} = 2.7013 \times 10^4$ EM for the CEM$_{43}$ and iCEM$_{43}$ dose models respectively, and $T_{crit} = 63.58$°C for the temperature threshold technique for Patient A, Slice 2:* ***(A)*** *ptgMRI and the damage regions predicted by* ***(B)*** *CEM$_{43}$,* ***(C)*** *iCEM$_{43}$, and* ***(D)*** *Temperature Threshold with their corresponding C_{DS} values.*

Table 4.2: *Results for all selected cases using the previously calculated average thresholds of* $t_{43,crit} = 1.0347 \times 10^7$ *and* $t'_{43,crit} = 2.7013 \times 10^4$ *Equivalent Minutes at* 43°C *and* $T_{crit} = 63.58$ °C.

Patient	Slice #	Normalized Dice Similarity Coefficient $N_{DS} = \dfrac{C_{DS}}{\bar{C}_{DS}}$		
		CEM_{43}	$iCEM_{43}$	Temperature Threshold
A	1	0.7864	0.8741	0.8480
	2	1.0909	1.0845	1.0882
	3	1.1272	1.0403	1.0743
	4	1.1342	1.0608	1.0883
B	5	1.0125	0.9491	0.9363
C	3	0.8624	0.8989	0.9214
D	4	1.0779	1.0365	1.0171
	5	1.0481	1.0369	1.0429
	6	0.7551	0.9757	1.0051
	7	1.0281	1.0107	0.9888
	8	1.0771	1.0325	0.9896
μ_a		1	1	1
σ_a		0.135	0.058	0.075

This second way of comparing consistency, also shows that when comparing the two thermal dose models, the $iCEM_{43}$ model out performs the CEM_{43} model, as evidenced by the σ_a values for both. The $iCEM_{43}$ thermal dose model has a σ_a value of 0.058, compared to a value of 0.135 for the CEM_{43} thermal dose model. Unlike with the first method of comparison, the $iCEM_{43}$ also seems to be slightly more consistent with this second test over the temperature threshold method as indicated by the σ_a value of 0.058 compared to 0.075. For results displayed in the same manner as **Figure 4.13** for all of the selected cases, please refer to **Appendix E**.

5. Discussion

Considering the selection criteria based on the C_{DS} value only Patients A and D can be looked at for consistency within a patient, as they are the only two which have multiple slices with C_{DS} values greater than 0.8. First, by simply looking at **Figure 4.4** and **Figure 4.10** the general consistency of each model across all slices for Patients A and D can be qualitatively seen. Since the end point for all of the slices is the same, immediate perfusion shutdown (on the order of minutes after the procedure), as shown in the ptgMRI scans, the dose threshold required for this damage should be the same across all slices, in an ideal case. When comparing the two thermal dose models, CEM_{43} and $iCEM_{43}$, the range of doses is far more consistent for the $iCEM_{43}$ as seen by fewer variations in the heights of the bars representing the dose threshold for each slice as compare to the graph for the CEM_{43} model. The temperature threshold method of damage determination shows even better consistency across the Patient A and D slices, as the fluctuations in the graph, although on a different scale, are relatively small.

Comparing the consistency across all patients is of even greater importance as it can be used to determine whether these models are patient dependant. In other words, does the dose required for a desired outcome vary amongst different patients when the desired outcome is the same for all patients? Having universal methods of damage monitoring and determination would allow for greater consistency in the planning and execution of thermal therapy procedures. If the required dose for the same end point is different between two patients, a predetermined threshold dose cannot be properly used. To compare the consistency of the CEM_{43}, $iCEM_{43}$, and temperature threshold methods, the two tests described in the previous section were utilized as well as qualitative visual analysis.

53

First, looking at the slices from all patients that met the selection criteria on the same axis for each model gives a good first impression of the consistency of each method. Since all slices for all patients used the same endpoint in the procedure, perfusion shutdown, all of the bars in each graph of **Figure 4.12** should be the same height, in an ideal world. With the results being presented in a normalized fashion, the graph with the most fluctuations about the mean value ($\mu = 1$), corresponds to the least consistent method. Considering this, there is much more fluctuation in **Figure 4.12(A)**, representing the CEM_{43} dose model than in **Figure 4.12(B)** representing the $iCEM_{43}$ dose model. When looking at **Figure 4.12(C)** it is also quite clear that the temperature threshold method showed fewer fluctuations than seen by either of the dose models. Thus, qualitatively speaking, it can be said that the $iCEM_{43}$ dose model is more consistent than the CEM_{43} dose model, and the temperature threshold is more consistent than both.

For a quantitative look into the consistency of these three methods of treatment monitoring and damage prediction, σ was found for the selected slices using the normalized results discussed. Looking at **Table 4.1**, the calculated σ values were 2.78, 0.700, and 0.178 for the CEM_{43}, $iCEM_{43}$, and temperature threshold techniques respectively. Considering these results, as expected from the qualitative analysis, the $iCEM_{43}$ dose model results are more consistent than those of the CEM_{43} dose model, and the temperature threshold technique results are the most consistent.

The third way to determine the consistency, and universality of the three methods was the use of the average threshold values for each technique found in this investigation. In essence this analysis is a way of simulating the procedures for all four patients, using a predetermined threshold dose value as determined from the results of the selected dose thresholds.

Furthermore, using the average values found in this investigation is a good first step in determining the best dose thresholds for each method for this particular procedure and endpoint (perfusion shutdown). For each of the 11 selected slices, the previously acquired maximum temperature and dose maps were used and any region with a value equal to or greater than the average threshold dose for each method was considered damaged. Looking at the normalized results as a whole and comparing the σ_a values for each method will provide good insight on the consistency and universality of the three methods. As seen in **Table 4.2**, using $t_{43,\text{crit}} = 1.0347 \times 10^7 \, EM$, $t'_{43,\text{crit}} = 2.7013 \times 10^4 \, \text{EM}$, and $T_{\text{crit}} = 63.58 \, ^\circ\text{C}$ (average threshold values), resulted in σ_a values of 0.135, 0.058, and 0.075, for the CEM$_{43}$, iCEM$_{43}$ dose models, and temperature threshold method, respectively. As with all of the previous forms of analysis, the CEM$_{43}$ thermal dose model is outperformed by the iCEM$_{43}$ model in terms of consistency as the iCEM$_{43}$ dose model has a smaller σ_a value. Unlike with the previous analysis, the iCEM$_{43}$ also shows greater consistency than the temperature threshold technique, albeit to a much smaller degree, in this test of consistency and universality.

As a whole, with both the qualitative and the two forms of quantitative analysis it is clearly evident that there is an increase in consistency when using the iCEM$_{43}$ dose model over the CEM$_{43}$. The temperature threshold appears to be the most consistent for this particular procedure, and more importantly endpoint, which can be expected. This can be explained by looking at the nature of the spatial gradients when considering the temperature threshold and thermal dose models. Typically, the temperature is at its highest at the center of heating (at the source), and decreases as you move outwards. Both dose models are exponential in nature, and thus when they are applied to a temperature profile it results in the steepening of the spatial gradient. Thus, when considering the first quantitative test predicting the dose from the spatial

55

damage it is expected that the dose models would have more variation in their predictions, because of the steepened profiles. Conversely, looking at the second quantitative test, the opposite relationship was used, predicting the spatial damage extent from a dose. Due to the exponential relationships in the dose models the steepened profiles results in greater consistency in the prediction of the spatial damage extent from a given dose. Furthermore, as you move away from the center of heating, the temperature spatial gradients drop, thus reducing the effect explained above. Therefore, dose models should be more useful in predicting the delayed damage in these regions. With respect to this delayed damage, the temperature data being used in this investigation did not include the cool down period following heating. Due to this lack of cool down temperature data, dose accumulation following the heating was not considered.

This procedure utilized rapid heating, over a short period of time, and more importantly the end point looked at was perfusion shutdown, immediately following the procedure. In the days following the procedure, additional cells will die and thus the damage region will actually grow. This type of damage is the result of cells being exposed to lower temperatures, which do not immediately coagulate tissue, but rather affect the proper functioning of cells. These cells will eventually die, and will increase the overall damage region. This happens further away from the laser insertion point, and it is the cumulative effect of having a smaller temperature increase over a length of time which leads to this sort of damage. It is at these periphery regions, and these prolonged effects where the temperature threshold technique is expected to falter and decrease in accuracy and consistency. In these outer regions, if a particular area reaches a temperature increase of about 5°C for less than a second damage may not occur. On the other hand, if a region experiences the same 5°C temperature increase, but it lasts for many minutes, damage may be expected. In a case such as this, the temperature threshold technique would not

predict damage, whereas the iCEM$_{43}$ and CEM$_{43}$ should. This is not a factor in the particular endpoint being considered in this thesis, however, for the same experiment if damage was looked at a week later, these prolonged effects would be present and the temperature threshold technique would not be suitable.

When comparing the CEM$_{43}$ and iCEM$_{43}$ thermal dose models it is important to look at when the iCEM$_{43}$ model is expected to outperform the CEM$_{43}$. If we consider **Figure 2.3**, both dose models are expected to perform similarly below ~54°C, which would be considered less intense longer duration types of procedures. The treatment being considered in this research involves much higher temperatures than 54°C, and it is no surprise that the iCEM$_{43}$ model outperforms the CEM$_{43}$. If we consider the prolonged effect as described previously, the cell death seen in the periphery would not have reached these high temperatures, thus the two models would perform more closely. Thus, the endpoint of perfusion shutdown is much better predicted by the iCEM$_{43}$ thermal dose model, whereas this superiority will not be as significant for prolonged cell death.

For this particular endpoint of this procedure, the temperature threshold technique does an acceptable job in predicting consistent results; however in the simulated procedure portion the iCEM$_{43}$ dose model was superior. If a different endpoint following the procedure was considered, such as cell death as opposed to perfusion shutdown, the iCEM$_{43}$ dose model would be expected to outperform the temperature threshold technique.

6. Conclusion and Future Work

6.1. Conclusions

The results shown in this investigation evaluated the consistency and universality of the two most widely used as well as a recently introduced treatment monitoring technique for thermal therapy. The two often used methods the CEM_{43} thermal dose model and temperature threshold differ in that the former utilizes temperature as it varies with time to predict thermal damage, whereas the latter uses temperature alone. The recently introduced $iCEM_{43}$ thermal dose model is similar to the CEM_{43} in that it utilized time and temperature; however the relationship used to associate this to thermal damage differs.

With the procedure and endpoint used in this investigation consistency was evaluated using two quantitative analysis techniques for all three techniques. The temperature threshold technique is the most consistent for the endpoint of perfusion shutdown used in this study. As explained previously, this was expected due to the nature of the procedure and the type of tissue death (immediate versus prolonged). When comparing the two thermal dose models which utilize both temperature and time there is a noticeable difference in the consistency of both dose the predictions, as well as damage volume predictions. The CEM_{43} dose model resulted in σ and σ_a values of 2.78 and 0.135, respectively as compared to 0.700 and 0.058 for the $iCEM_{43}$ dose model.

With these findings, it can be concluded that for this laser interstitial thermal therapy to treat low-grade prostate cancer the recently introduced $iCEM_{43}$ thermal dose model is clearly more consistent the current CEM_{43} model. Furthermore, considering the endpoint used in this

investigation (perfusion shutdown) the temperature threshold is the most consistent monitoring technique. These conclusions can only be made for this procedure and the particular endpoint of perfusion shutdown.

6.2. Future Work

For the work shown in this thesis only 11 slices across all patients were used, given more time, more slices could have been analyzed using interpolation to include slices for which temperature and ptgMRI scans are not currently in agreement with respect to slice location. Further investigations of a similar nature for additional procedures, and endpoints should be performed to further evaluate the consistency of the three methods. In particular, utilizing an endpoint which takes into consideration the prolonged effects of thermal therapy as opposed to only the acute effects would be very beneficial. For the procedure described in this work, using post-treatment MRI scans in the subsequent days following the procedure could provide insight into the consistency of the three methods of dose prediction for these prolonged thermal effects. Lastly, by performing this type of analysis on more patients for this procedure, as well as for other procedures and endpoints, it will allow for the determination of better threshold doses for all of the three methods and the different endpoints. By determining better threshold doses for all of the methods, accuracy of procedures using any of the methods would be increased.

7. Appendix A
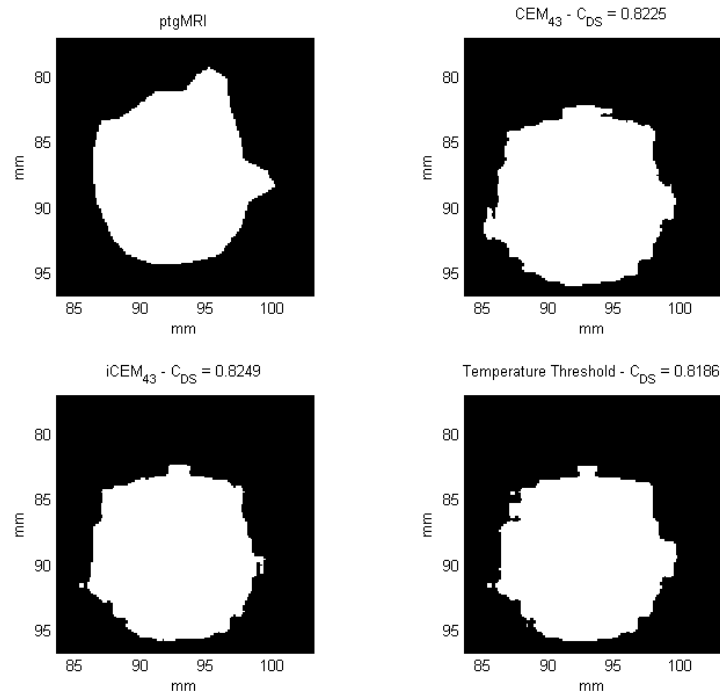
Figure 7.1: *Results for Patient A, Slice 1*
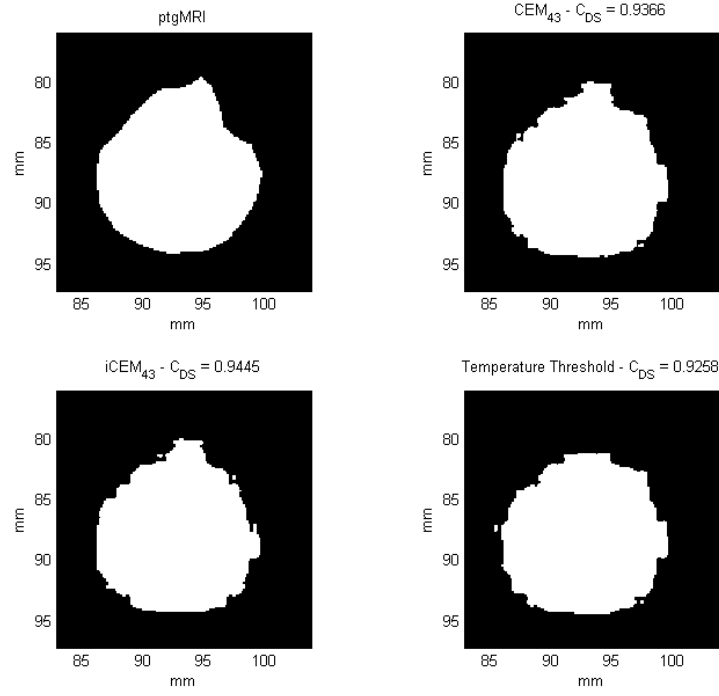
Figure 7.2: *Results for Patient A, Slice 2*
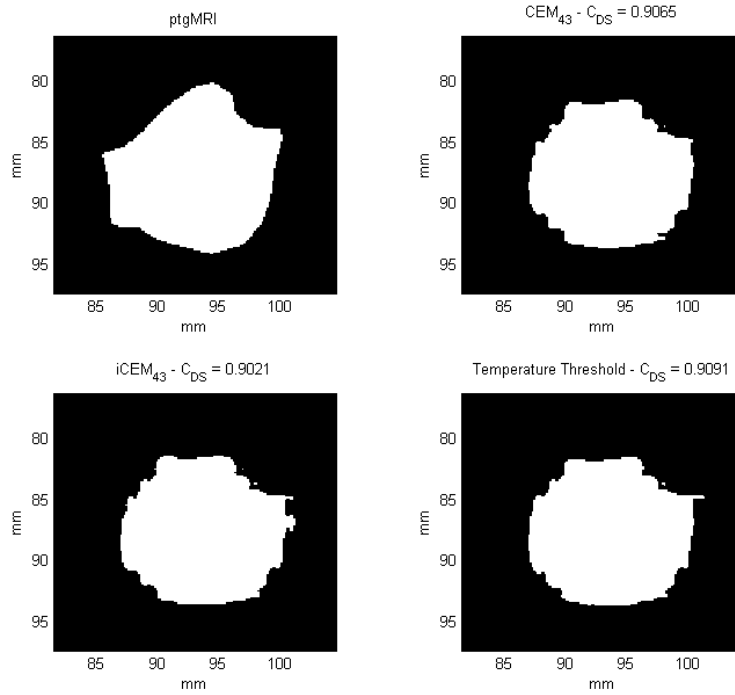
Figure 7.3: *Results for Patient A, Slice 3*
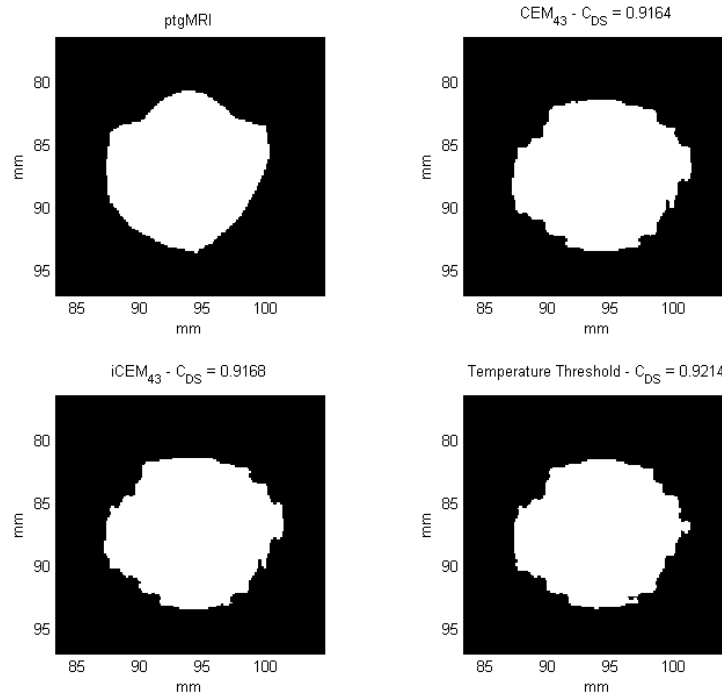
Figure 7.4: *Results for Patient A, Slice 4*
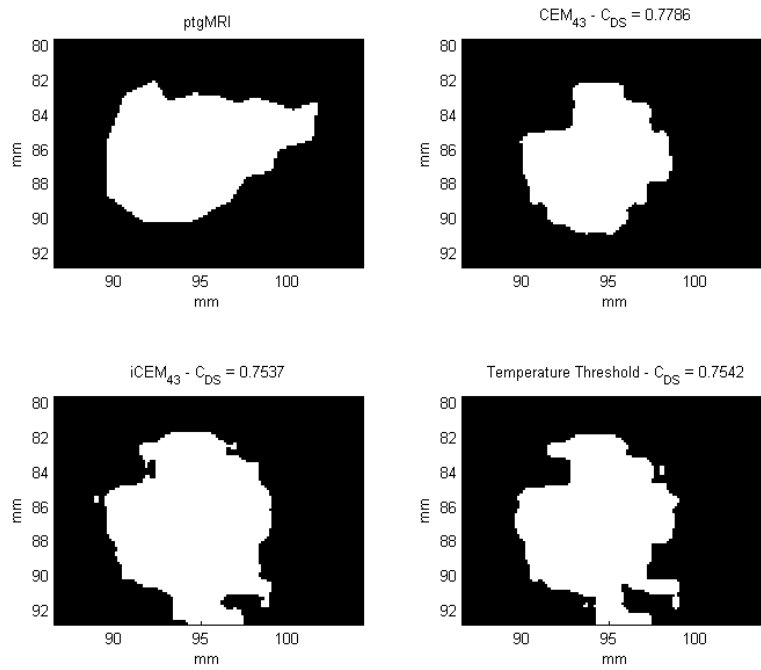
Figure 7.5: *Results for Patient A, Slice 5*

8. Appendix B
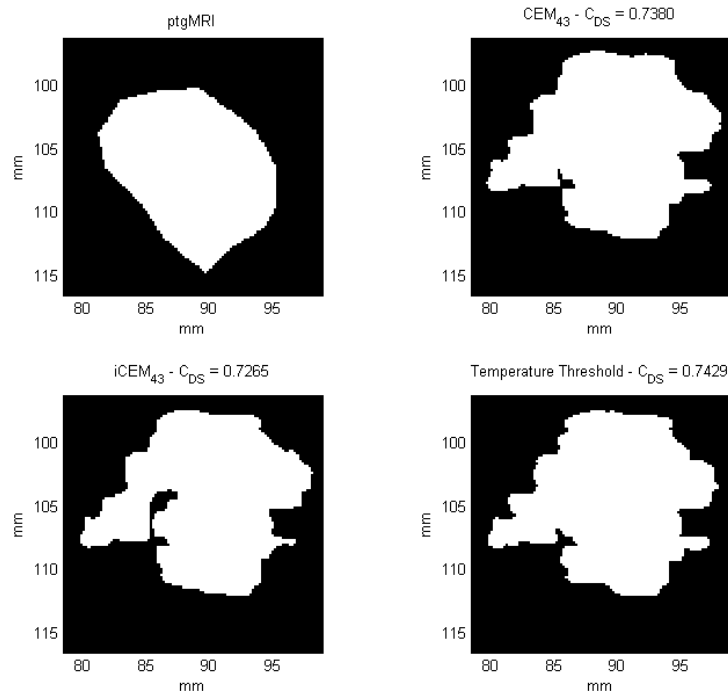
Figure 8.1: *Results for Patient B, Slice 1*
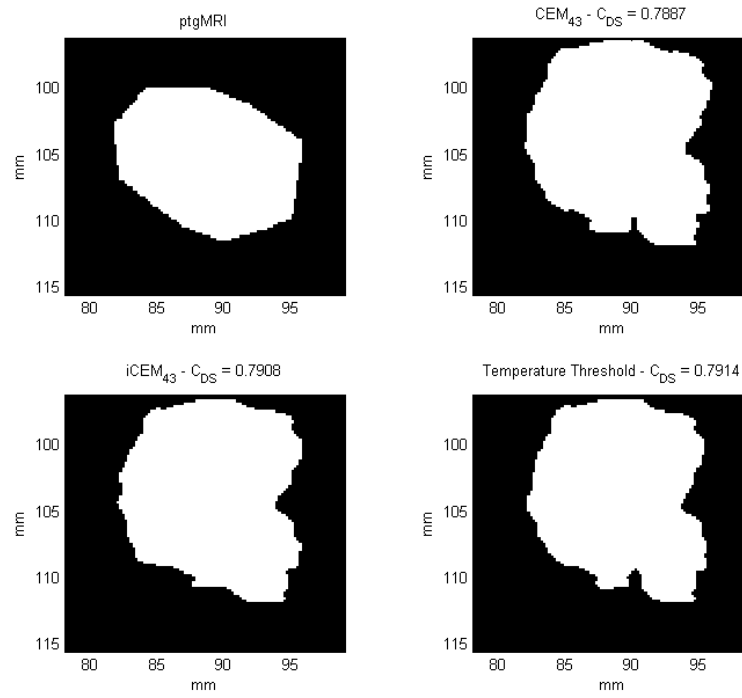
Figure 8.2: *Results for Patient B, Slice 2*
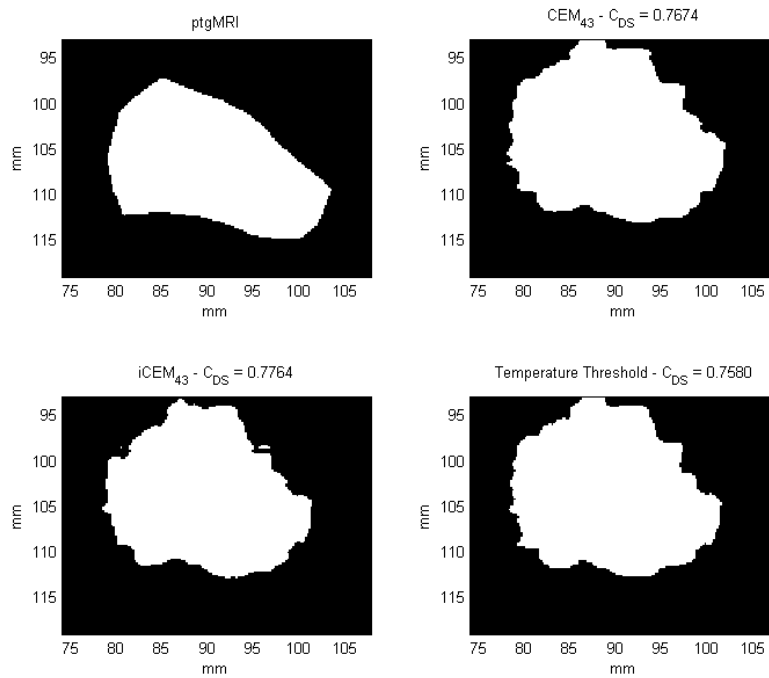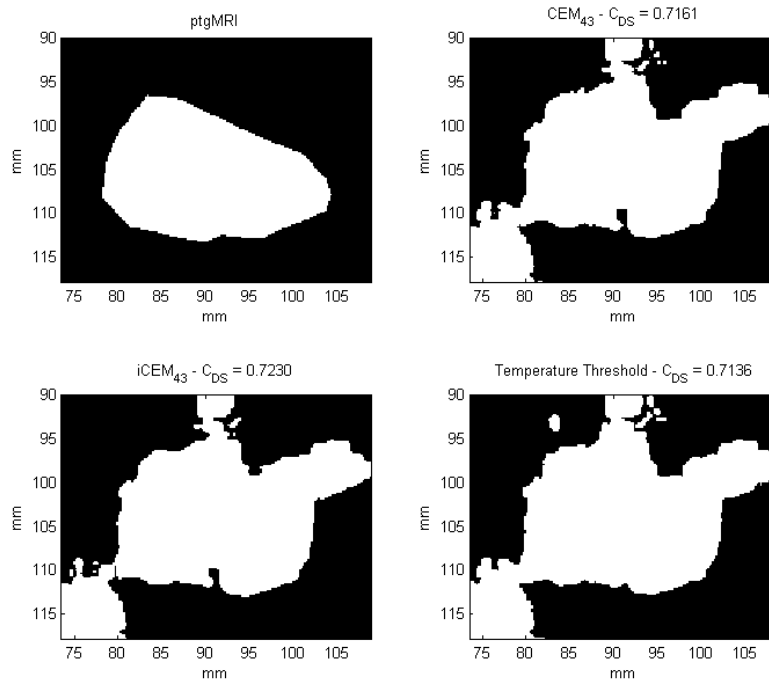

Figure 8.3: *Results for Patient B, Slice 3*

Figure 8.4: *Results for Patient B, Slice 4*
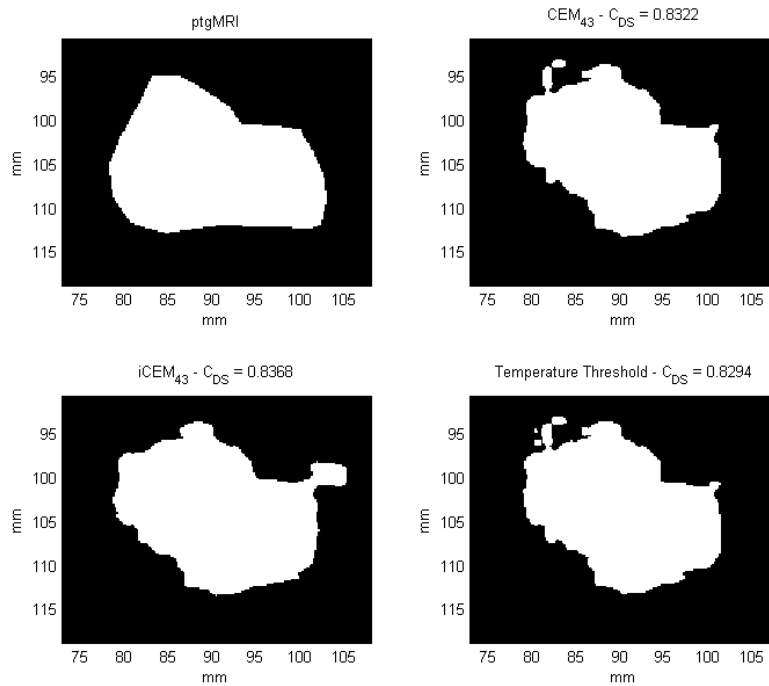
Figure 8.5: *Results for Patient B, Slice 5*
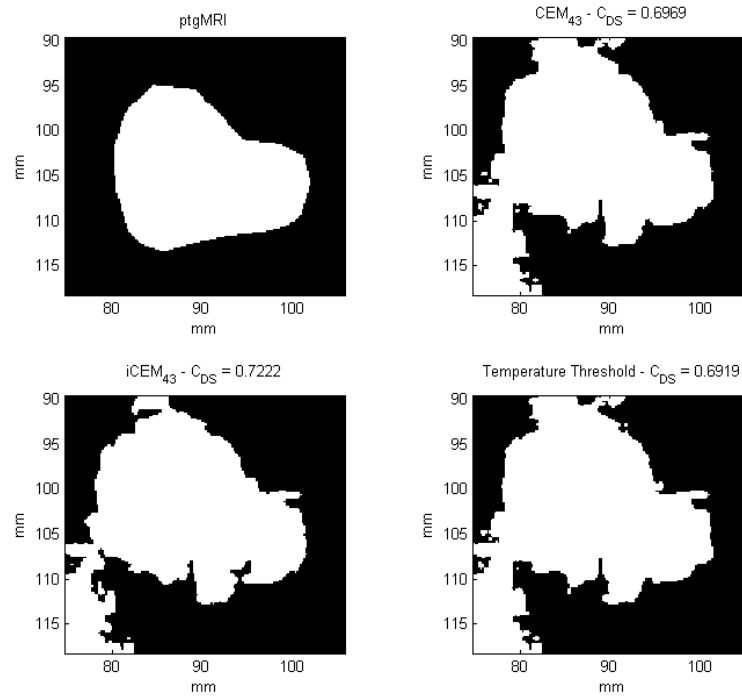
Figure 8.6: *Results for Patient B, Slice 6*
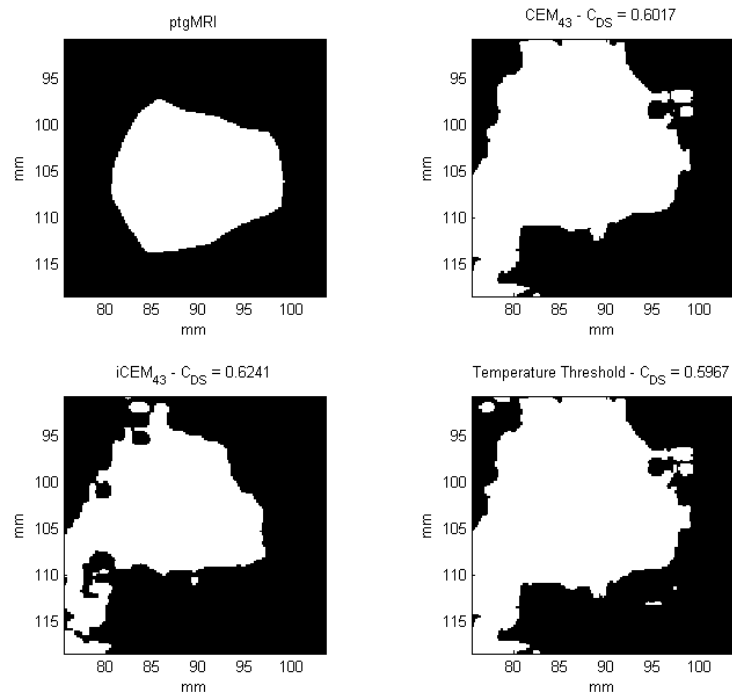
Figure 8.7: *Results for Patient B, Slice 7*
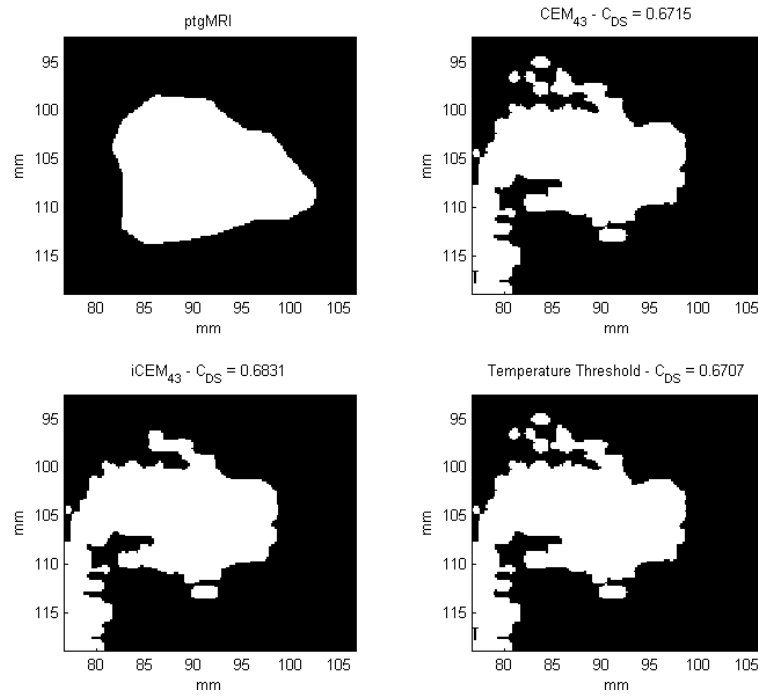
Figure 8.8: *Results for Patient B, Slice 8*

9. Appendix C
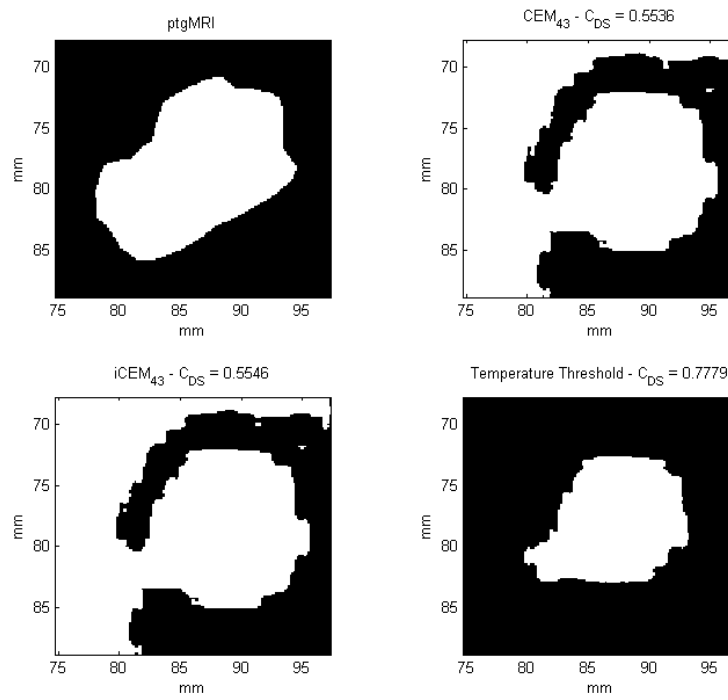
Figure 9.1: *Results for Patient C, Slice 1*
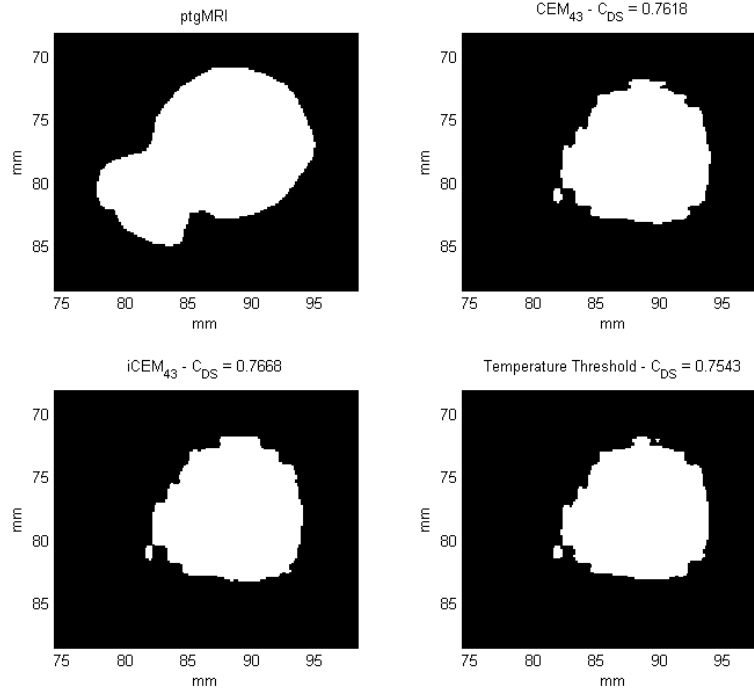
Figure 9.2: *Results for Patient C, Slice 2*
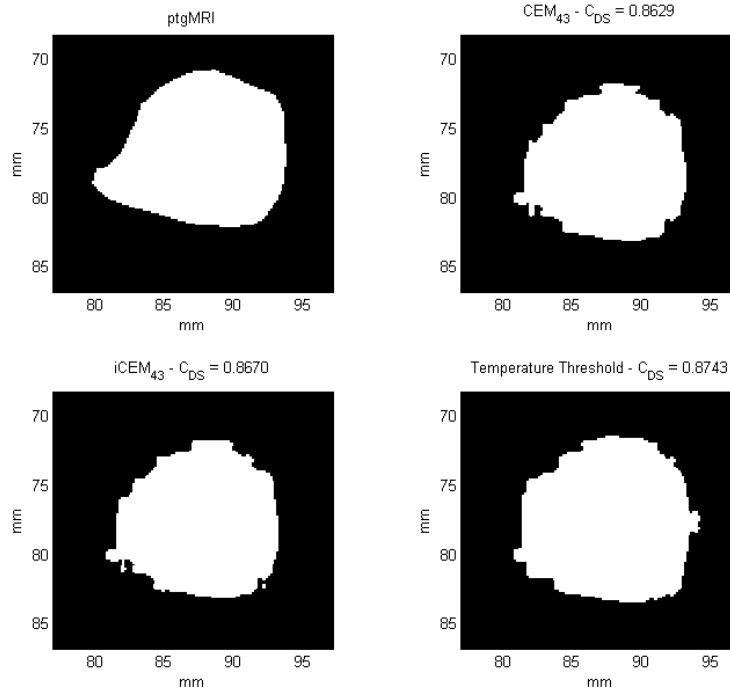
Figure 9.3: *Results for Patient C, Slice 3*
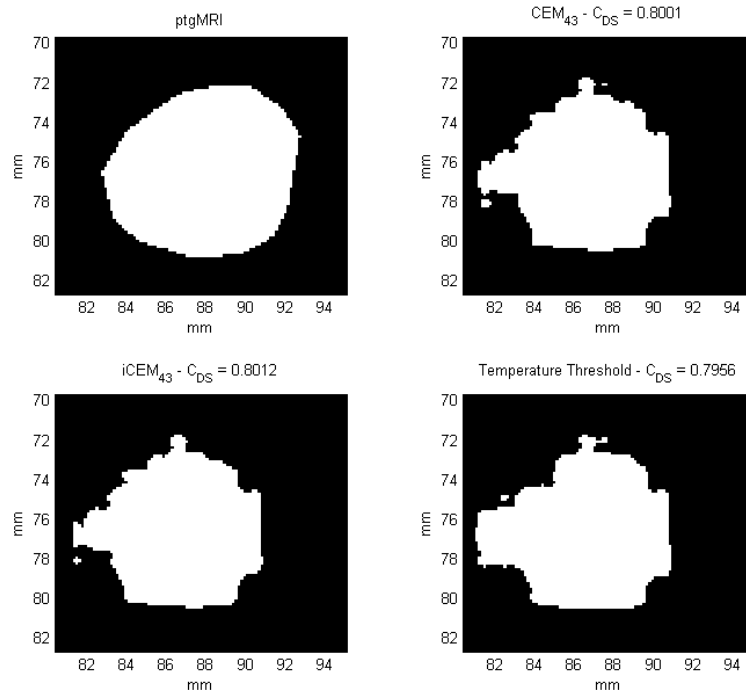
Figure 9.4: *Results for Patient C, Slice 4*

10. Appendix D
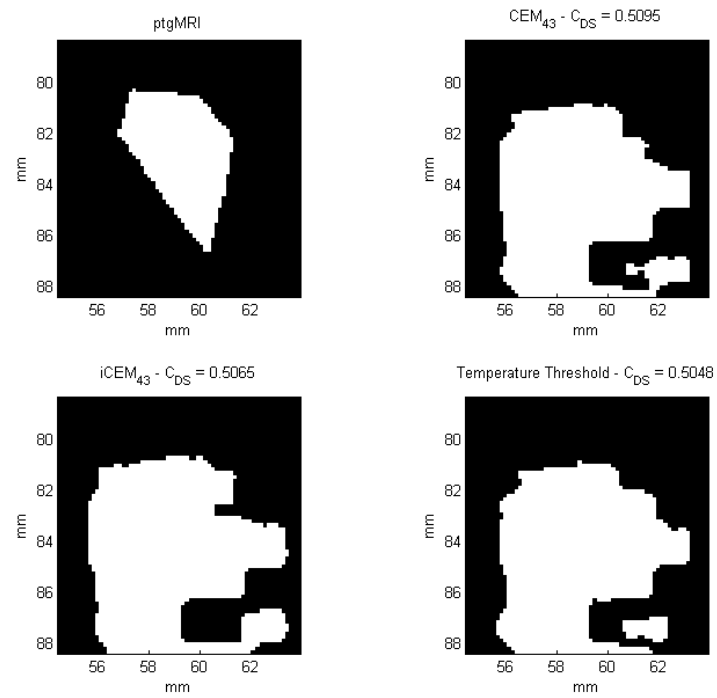
Figure 10.1: *Results for Patient D, Slice 1*
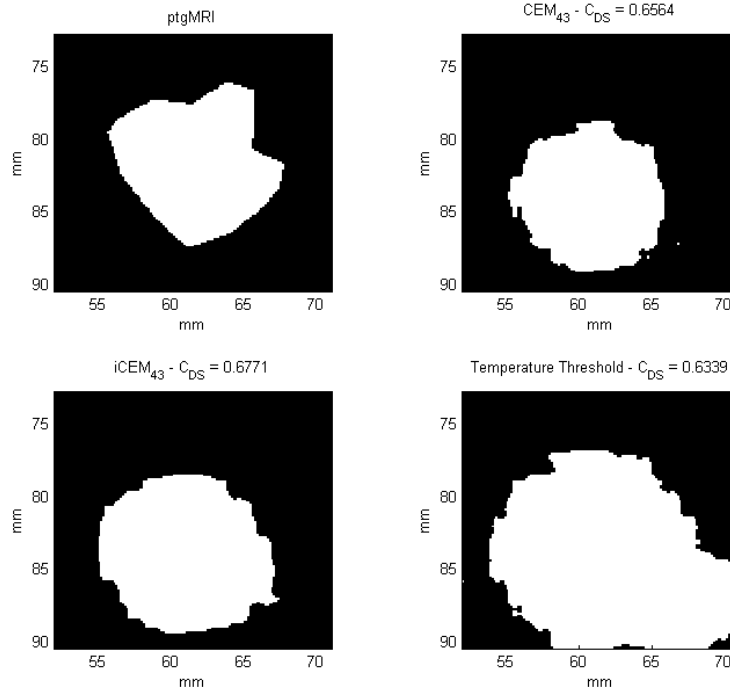
Figure 10.2: *Results for Patient D, Slice 2*
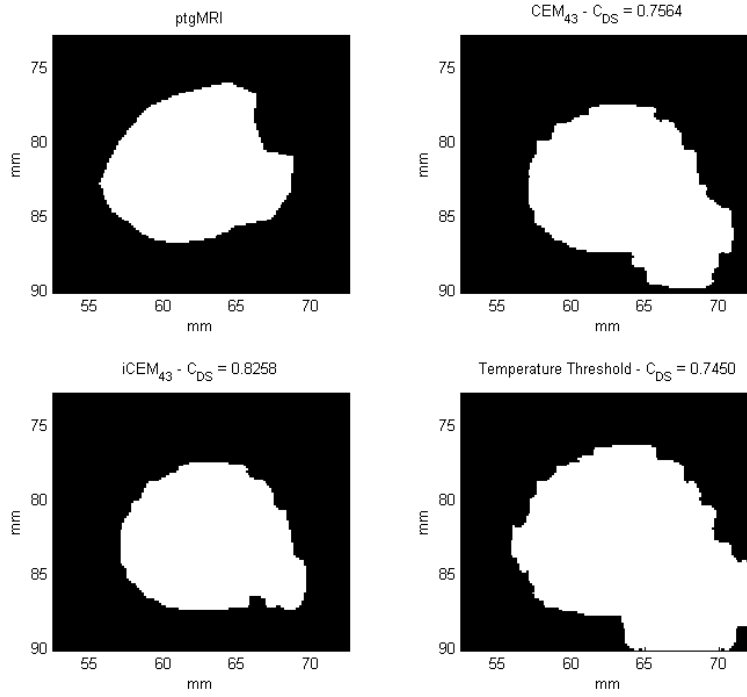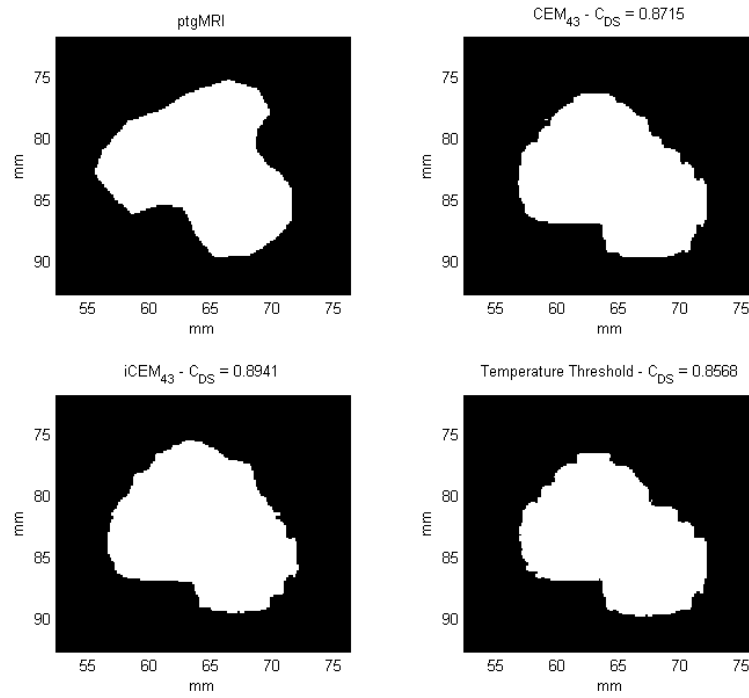

Figure 10.3: *Results for Patient D, Slice 3*

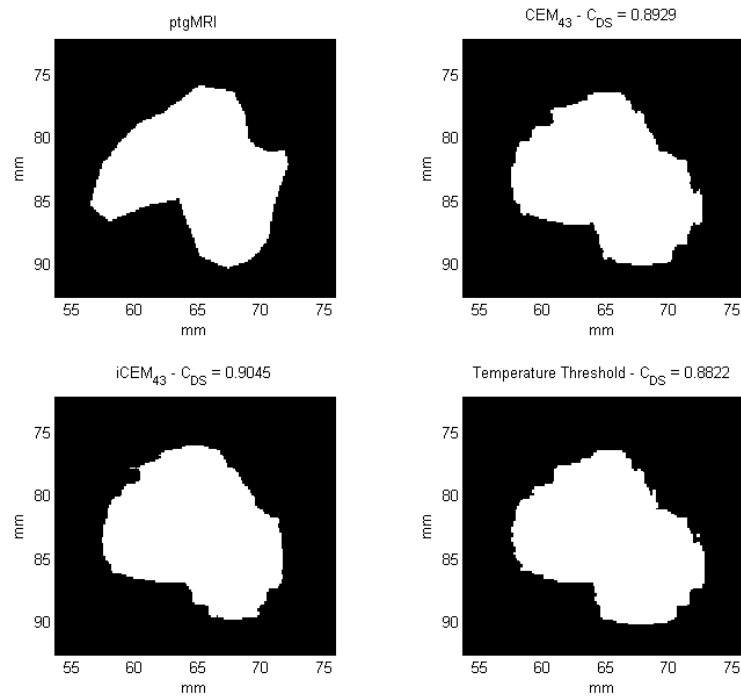**Figure 10.4:** *Results for Patient D, Slice 4*

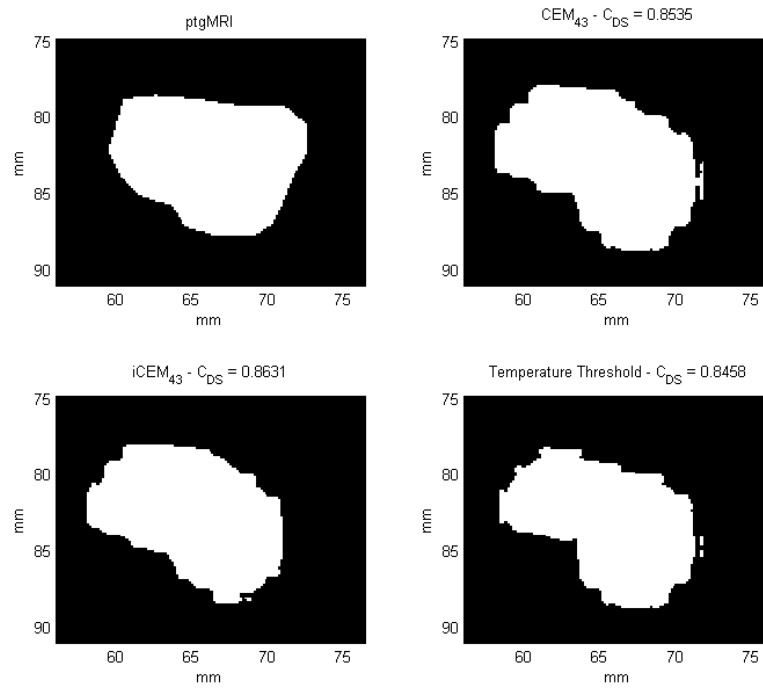**Figure 10.5:** *Results for Patient D, Slice 5*

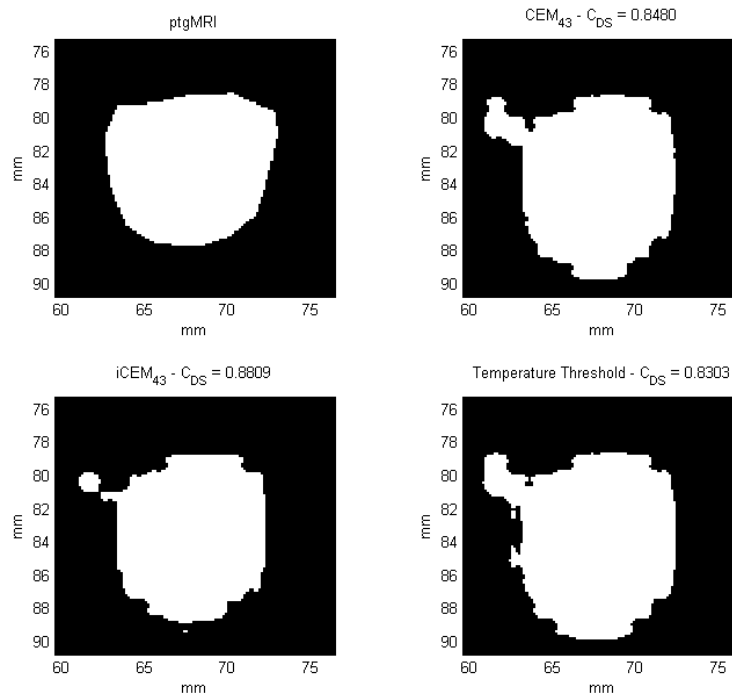**Figure 10.6:** *Results for Patient D, Slice 6*

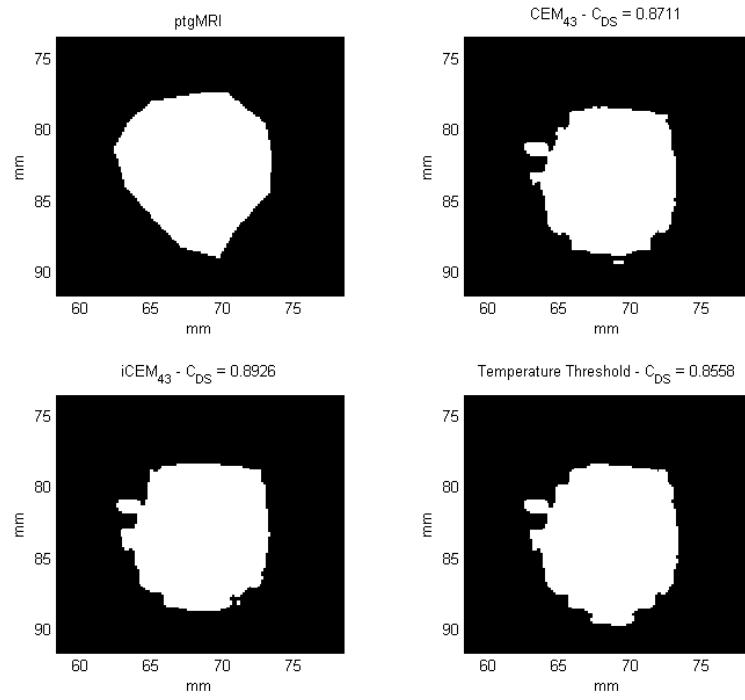**Figure 10.7:** *Results for Patient D, Slice 7*

Figure 10.8: *Results for Patient D, Slice 8*

11. Appendix E

Figure 11.1: *Results of damage region prediction using the average dose thresholds for all three methods for Patient A, Slice 1*
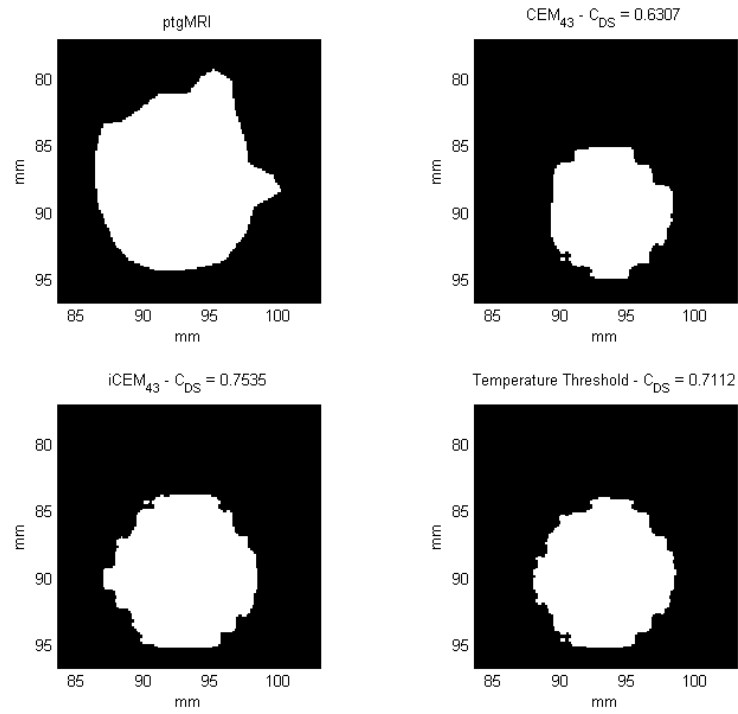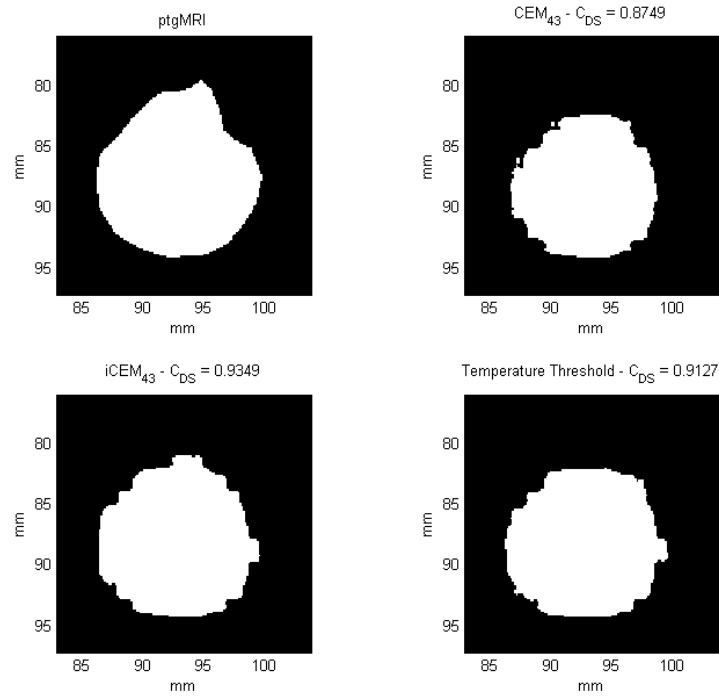
Figure 11.2: Results of damage region prediction using the average dose thresholds for all three methods for Patient A, Slice 2

Figure 11.3: Results of damage region prediction using the average dose thresholds for all three methods for Patient A, Slice 3

Figure 11.4: *Results of damage region prediction using the average dose thresholds for all three methods for Patient A, Slice 4*

Figure 11.5: *Results of damage region prediction using the average dose thresholds for all three methods for Patient B, Slice 5*

Figure 11.6: *Results of damage region prediction using the average dose thresholds for all three methods for Patient C, Slice 3*
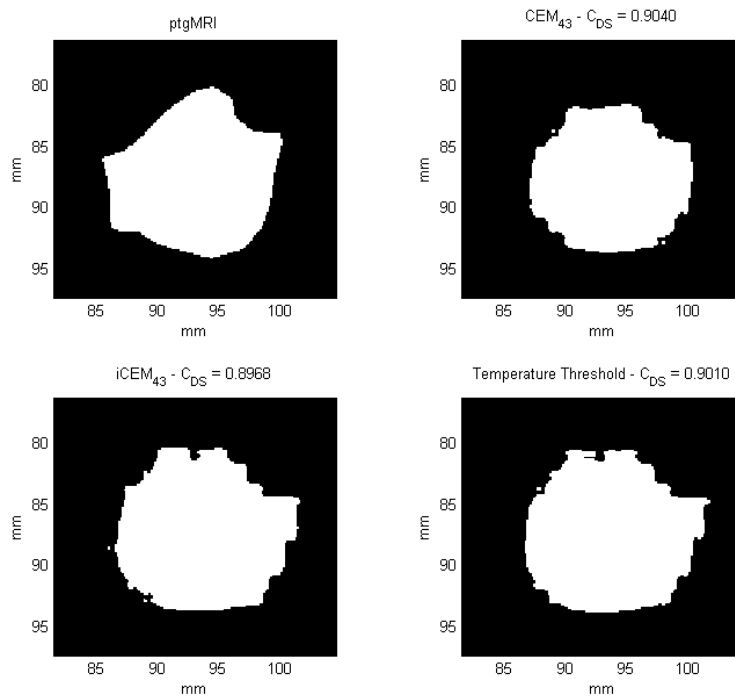

Figure 11.7: *Results of damage region prediction using the average dose thresholds for all three methods for Patient D, Slice 4*

Figure 11.8: *Results of damage region prediction using the average dose thresholds for all three methods for Patient D, Slice 5*
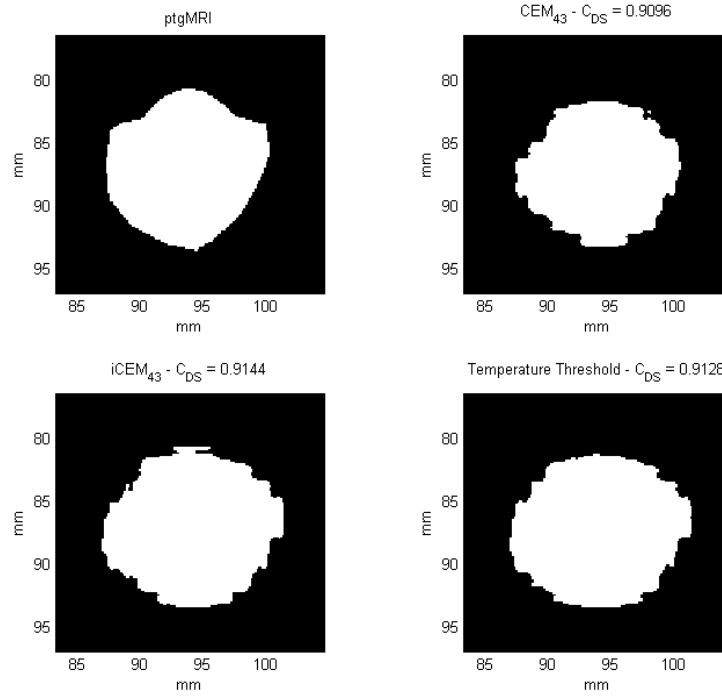

Figure 11.9: *Results of damage region prediction using the average dose thresholds for all three methods for Patient D, Slice 6*
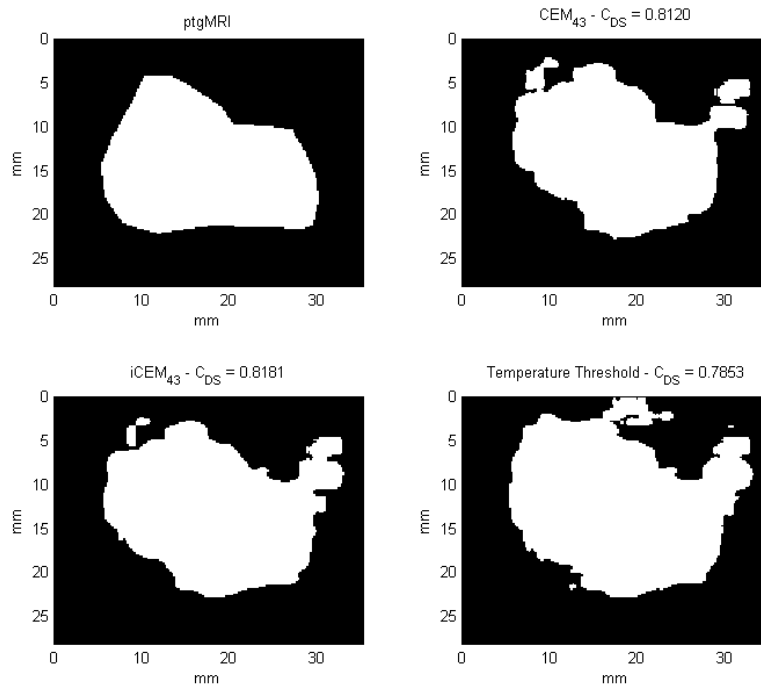
Figure 11.10: *Results of damage region prediction using the average dose thresholds for all three methods for Patient D, Slice 7*
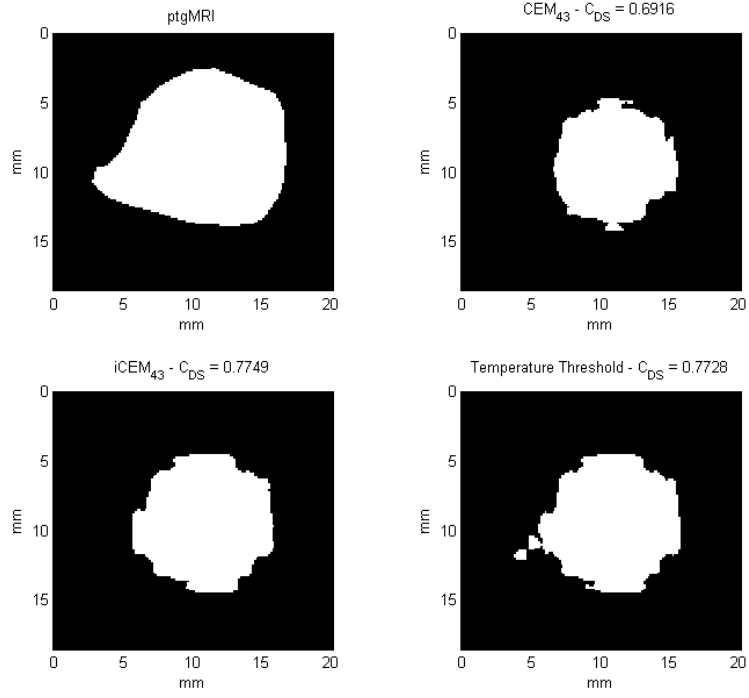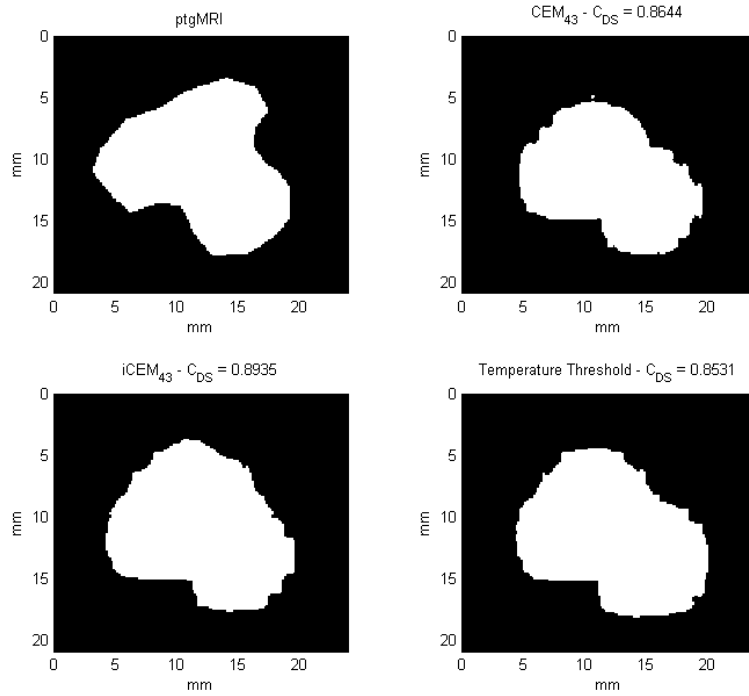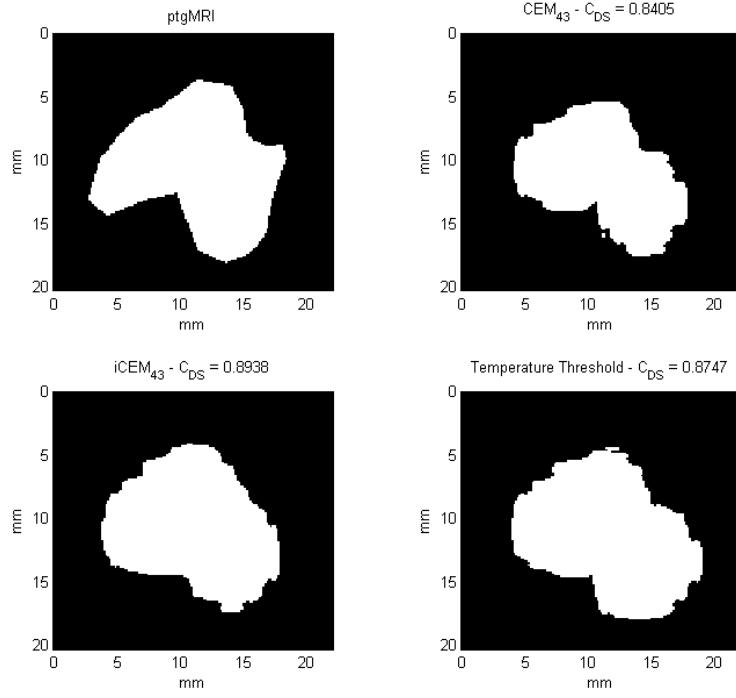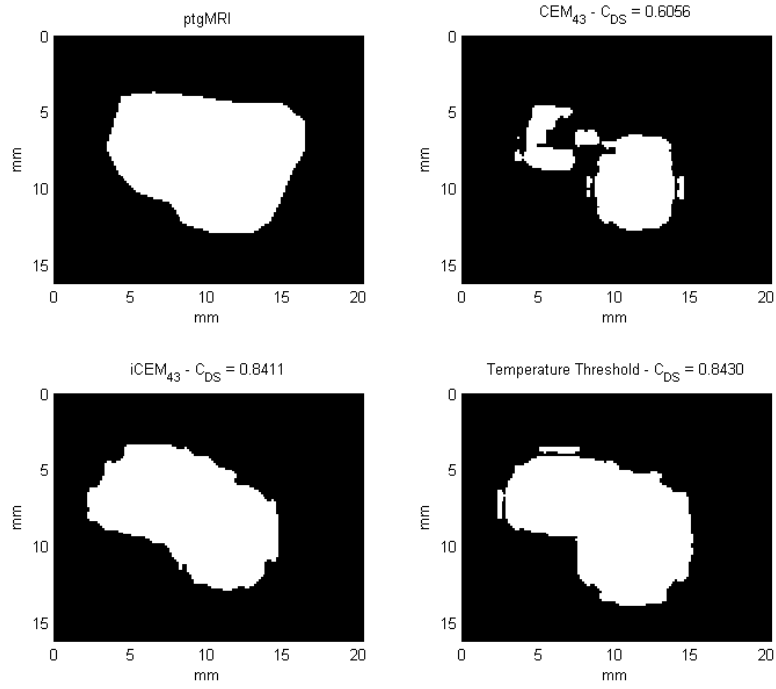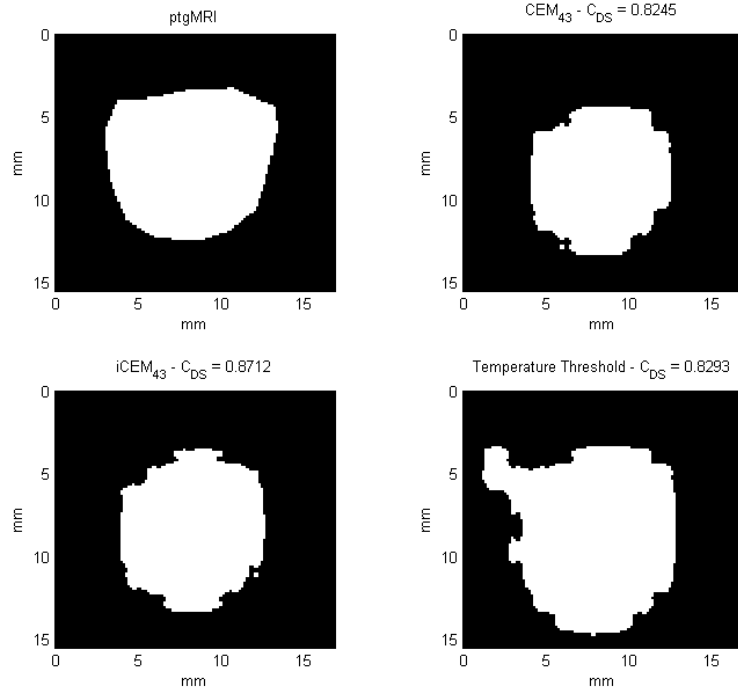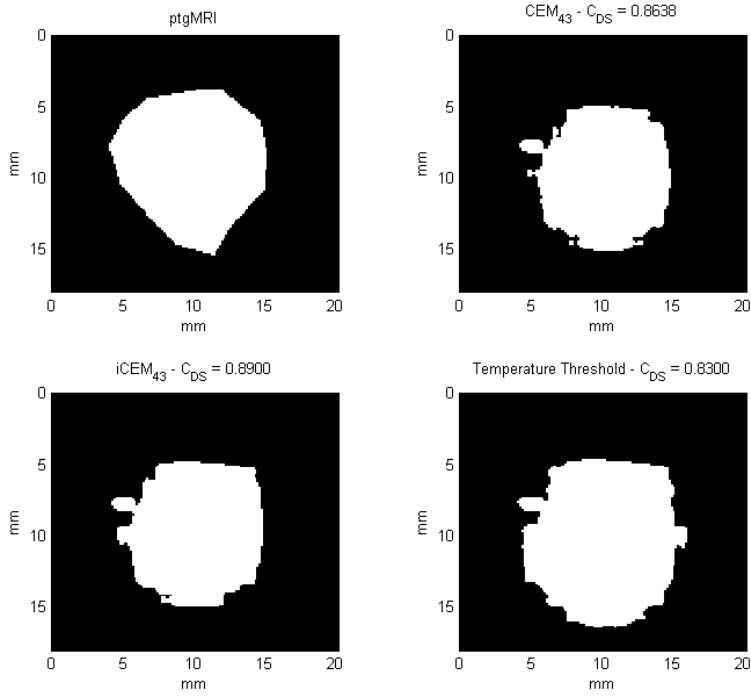

Figure 11.11: *Results of damage region prediction using the average dose thresholds for all three methods for Patient D, Slice 8*

81

Bibliography

[1]   "Prostate Cancer," *Prostate Cancer Canada*, 2011. [Online]. Available: http://www.prostatecancer.ca/Prostate-Cancer. [Accessed: 14-Sep-2012].

[2]   "Treatment Options," *Prostate Cancer Canada*, 2011. [Online]. Available: http://www.prostatecancer.ca/Prostate-Cancer/Basics-on-Treatment/Treatment-Options. [Accessed: 15-Sep-2012].

[3]   K. Siddiqui, R. Chopra, S. Vedula, L. Sugar, M. Haider, A. Boyes, M. Musquera, M. Bronskill, and L. Klotz, "MRI-guided Transurethral Ultrasound Therapy of the Prostate Gland Using Real-Time Thermal Mapping: Initial Studies," *Urology*, vol. 76, no. 6, pp. 1506–1511, Dec. 2010.

[4]   E. R. Cordeiro, X. Cathelineau, S. Thüroff, M. Marberger, S. Crouzet, and J. J. M. C. H. de la Rosette, "High-intensity focused ultrasound (HIFU) for definitive treatment of prostate cancer," *BJU international*, vol. 110, no. 9, pp. 1228–1242, Nov. 2012.

[5]   U. Lindner, R. A. Weersink, M. A. Haider, M. R. Gertner, S. R. H. Davidson, M. Atri, B. C. Wilson, A. Fenster, and J. Trachtenberg, "Image Guided Photothermal Focal Therapy for Localized Prostate Cancer: Phase I Trial," *The Journal of Urology*, vol. 182, no. 4, pp. 1371–7, Oct. 2009.

[6]   W. C. Dewey, L. E. Hopwood, S. A. Sapareto, and L. E. Gerweck, "Cellular Responses to Combinations of Hyperthermia and Radiation," *Radiology*, vol. 123, no. 2, pp. 463–474, 1977.

[7]   W. M. Whelan and D. R. Wyman, "Dynamic Modeling of Interstitial Laser Photocoagulation: Implications for Lesion Formation in Liver In Vivo," *Lasers in Surgery and Medicine*, vol. 24, no. 3, pp. 202–8, Jan. 1999.

[8]   D. Haemmerich and P. F. Laeseke, "Thermal tumour ablation: Devices, clinical applications and future directions," *International Journal of Hyperthermia*, vol. 21, no. 8, pp. 755–60, Dec. 2005.

[9]   O. Raz, M. A. Haider, S. R. H. Davidson, U. Lindner, E. Hlasny, R. Weersink, M. R. Gertner, W. Kucharczyk, S. A. McCluskey, and J. Trachtenberg, "Real-Time Magnetic Resonance Imaging-Guided Focal Laser Therapy in Patients with Low-Risk Prostate Cancer," *European Urology*, vol. 58, no. 1, pp. 173–7, Jul. 2010.

[10]   H. Assi, *A New CEM43 Thermal Dose Model Based on Vogel-Tammann-Fulcher Behaviour in Thermal Damage Process*. M. Sc. Thesis: Ryerson University, 2009.

[11] M. R. Gertner, B. C. Wilson, and M. D. Sherar, "Ultrasound Properties of Liver Tissue During Heating," *Ultrasound in Medicine & Biology*, vol. 23, no. 9, pp. 1395–1403, 1997.

[12] J. Heisterkamp, R. van Hillegersberg, and J. N. Ijzermans, "Interstitial laser coagulation for hepatic tumours," *The British Journal of Surgery*, vol. 86, no. 3, pp. 293–304, Mar. 1999.

[13] T. G. Purdie, T. Y. Lee, M. Iizuka, and M. D. Sherar, "Dynamic Contrast Enhanced CT Measurement of Blood Flow During Interstitial Laser Photocoagulation: Comparison with an Arrhenius Damage Model," *Physics in Medicine and Biology*, vol. 45, no. 5, pp. 1115–1126, May 2000.

[14] W. M. Whelan, S. R. H. Davidson, L. C. L. Chin, and I. A. Vitkin, "A Novel Strategy For Monitoring Laser Thermal Therapy Based on Changes in Optothermal Properties of Heated Tissues," *International Journal of Thermophysics*, vol. 26, no. 1, pp. 233–241, Jan. 2005.

[15] D. Arora, D. Cooley, T. Perry, M. Skliar, and R. B. Roemer, "Direct Thermal Dose Control of Constrained Focused Ultrasound Treatments: Phantom and In Vivo Evaluation," *Physics in Medicine and Biology*, vol. 50, no. 8, pp. 1919–1935, Apr. 2005.

[16] E. Samset, "Temperature mapping of thermal ablation using MRI," *Minimally Invasive Therapy*, vol. 15, no. 1, pp. 36–41, Jan. 2006.

[17] L. Chen, J. P. Wansapura, G. Heit, and K. Butts, "Study of Laser Ablation in the In Vivo Rabbit Brain With MR Thermometry," *Journal of Magnetic Resonance Imaging*, vol. 16, no. 2, pp. 147–152, Aug. 2002.

[18] S. Chavez, Q. Xiang, and L. An, "Understanding Phase Maps in MRI: A New Cutline," *IEEE Transactions on Medical Imaging*, vol. 21, no. 8, pp. 966–977, 2002.

[19] Y. Ishihara, A. Calderon, H. Watanabe, K. Okamoto, Y. Suzuki, and K. Kuroda, "A precise and Fast Temperature Mapping Using Water Proton Chemical Shift," *Magnetic Resonance in Medicine*, vol. 34, no. 6, pp. 814–823, Dec. 1995.

[20] K. Ahrar and R. J. Stafford, "Magnetic Resonance Imaging-Guided Laser Ablation of Bone Tumors," *Techniques in Vascular and Interventional Radiology*, vol. 14, no. 3, pp. 177–82, Sep. 2011.

[21] S. Sapareto and W. C. Dewey, "Thermal Dose Determination in Cancer Therapy," *Internation Journal of Radiation Oncology*, vol. 10, pp. 787–800, Apr. 1984.

[22] N. McDannold, K. Hynynen, D. Wolf, G. Wolf, and F. Jolesz, "MRI Evaluation of Thermal Ablation of Tumors with Focused Ultrasound," *Journal of Magnetic Resonance Imaging*, vol. 8, no. 1, pp. 91–100, 1998.

[23] A. H. Chung, F. A. Jolesz, and K. Hynynen, "Thermal Dosimetry of a Focused Ultrasound Beam in Vivo by Magnetic Resonance Imaging," *Meidcal Physics*, vol. 26, no. 9, pp. 2017–2026, 1999.

[24] M. W. Miller and M. C. Ziskin, "Biological Consequences of Hyperthermia," *Ultrasound in Medicine & Biology*, vol. 15, no. 8, pp. 707–722, Jan. 1989.

[25] A. R. Moritz and F. C. Henriques, "Studies of Thermal Injury: II. The Relative Importance of Time and Surface Temperature in the Causation of Cutaneous Burns," *American Journal of Pathology*, vol. 23, no. 5, pp. 695–720, 1947.

[26] D. P. Cann, C. A. Randall, and T. R. Shrout, "Investigation of the Dielectric Properties of Bismuth Pyrochlores," *Solid State Communications*, vol. 100, no. 7, pp. 529–534, 1996.

[27] F. Civan, "Applicability of the Vogel-Tammann-Fulcher type asymptotic exponential functions for ice, hydrates, and polystyrene latex," *Journal of Colloid and Interface Science*, vol. 285, no. 1, pp. 429–432, May 2005.

[28] K. D. Bauer and K. J. Henle, "Arrhenius Analysis of Heat Survival Curves from Normal and Thermotolerant CHO Cells," *Radiation Research*, vol. 78, no. 2, pp. 251–63, May 1979.

[29] H. A. Johnson and M. Pavelec, "Thermal Injury due to Normal Body Temperature," *American Journal of Pathology*, vol. 66, no. 3, pp. 557–564, 1972.

[30] P. Ross-Riveros and J. T. Leith, "Response of 9L Tumor Cells to Hyperthermia X Irradiation," *Radiation Research*, vol. 78, no. 2, pp. 296–311, 1979.

[31] F. C. Henriques, "Studies of Thermal Injury: V. The Predictability and the Significance of Thermally Induced Rate Processes Leading to Irreversible Epidermal Injury," *Archives of Pathology*, vol. 43, no. 5, pp. 489–502, May 1947.

[32] H. S. Reinhold and A. Van Den Berg-Blok, "The Influence of a Heat Pulse on the Thermally Induced Damage to Tumour Microcirculation," *European Journal of Cancer and Clinical Oncology*, vol. 19, no. 2, pp. 221–225, 1983.

[33] J. P. Yung, A. Shetty, A. Elliott, J. S. Weinberg, R. J. McNichols, A. Gowda, J. D. Hazle, and R. J. Stafford, "Quantitative comparison of thermal dose models in normal canine brain," *Medical Physics*, vol. 37, no. 10, p. 5313, 2010.

[34] M. Sussman, "Errors in Temperature Mapping Data : Feb 14 , 2012." Personal Communication, Toronto, 2012.

[35] M. Viallon, S. Terraz, J. Roland, E. Dumont, C. Becker, and R. Salomir, "Observation and Correction of Transient Cavitation-Induced PRFS Thermometry Artifacts During

Radiofrequency Ablation, Using Simultaneous Ultrasound/MR Imaging," *Medical Physics*, vol. 37, no. 4, pp. 1491–1506, 2010.